Comparison of the mechanobiological performance of bone tissue scaffolds based on different unit cell geometries

Link to publisher version with DOI

https://doi.org/10.1016/j.jmbbm.2018.04.008

Comparison of the Mechanobiological Performance of Bone Tissue Scaffolds Based on Different Unit Cell Geometries

Óscar L. Rodríguez-Montaño[1,2], Carlos Julio Cortés-Rodríguez[1], Antonio E. Uva[2], Michele Fiorentino[2], Michele Gattullo[2], Giuseppe Monno[2], Antonio Boccaccio[2]*

[1] Biomechanics Research Group, Departamento de Ingeniería Mecánica y Mecatrónica, Facultad de Ingeniería, Universidad Nacional de Colombia, Colombia

[2] Dipartimento di Meccanica, Matematica e Management, Politecnico di Bari, Bari 70126, Italy

*Corresponding author:

Mailing Address:

Dipartimento di Meccanica, Matematica e Management

Politecnico di Bari

Viale Japigia, 182

70126, Bari

Italy

Contact Information:

Tel: +39-0805962705

Fax: +39-0805962777

E-mail: a.boccaccio@poliba.it

Abstract

Enhancing the performance of scaffolds for bone regeneration requires a multidisciplinary approach involving competences in the fields of Biology, Medicine and Engineering. A number of studies have been conducted to investigate the influence of scaffolds design parameters on their mechanical and biological response. The possibilities offered by the additive manufacturing techniques to fabricate sophisticated and very complex microgeometries that until few years ago were just a geometrical abstraction, led many researchers to design scaffolds made from different unit cell geometries. The aim of this work is to find, based on mechanobiological criteria and for different load regimes, the optimal geometrical parameters of scaffolds made from beam-based repeating unit cells, namely, truncated cuboctahedron, truncated cube, rhombic dodecahedron and diamond. The performance, -expressed in terms of percentage of the scaffold volume occupied by bone-, of the scaffolds based on these unit cells was compared with that of scaffolds based on other unit cell geometries such as: hexahedron and rhombicuboctahedron. A very intriguing behavior was predicted for the truncated cube unit cell that allows the formation of large amounts of bone for low load values and of very small amounts for the medium-high ones. For high values of load, scaffolds made from hexahedron unit cells were predicted to favor the formation of the largest amounts of bone. In a clinical context where medical solutions become more and more customized, this study offers a support to the surgeon in the choice of the best scaffold to be implanted in a patient-specific anatomic region.

Keywords: Beam-Based Scaffolds; Bone Tissue Engineering; Mechanobiology; Unit Cell; Rhombic Dodecahedron; Truncated Cube; Truncated Cuboctahedron; Diamond.

1. Introduction

Bone tissue loss by trauma or disease can produce critical size defects that cannot heal spontaneously thus requiring the implantation of bone substitutes (El-Rashidy et al., 2017). A very promising and commonly adopted strategy to replace the lost bone tissue is the use of scaffolds for bone regeneration. There is evidence that geometrical and mechanical properties of bone scaffolds influence the behavior and the response of regenerated tissue (Murphy et al., 2013). Different properties such as the pore size and shape, the porosity, the Young's modulus of the material the scaffold is made from, are utilized as design parameters to optimize the scaffold performance (Polo-Corrales et al., 2014).

Depending on the fabrication technique utilized, it is possible to have a more or less precise control of the scaffold micro-geometrical features. For instance, the chemical processes using the foaming methods to produce porous materials allow to control just the average pore size and porosity but cannot guarantee the control of specific geometrical features such as the pore shape and size as well as the interconnectivity (Loh and Choong, 2013; Wang, Xu, et al., 2016). Other manufacturing techniques such as freeze-drying and space holders present the same limitations (Bose et al., 2013). 3D printing techniques, instead, allow the control of the generated geometry with an accuracy which depends on the resolution of the device utilized for fabrication (Loh and Choong, 2013). Thanks to the advantages provided by the additive manufacturing methods, it is possible to produce scaffolds with specific topologies (Wang, Xu, et al., 2016; Bobbert et al., 2017). Among the different porous materials currently fabricated, those based on unit cells with a specific geometry can be built with high precision as well as their mechanical behavior can be predicted with high accuracy unlike those with irregular geometry (Ahmadi et al., 2015).

Different studies have been proposed in the literature that suggest sophisticated micro-architectures for unit cell scaffolds (Kang et al., 2010; Ahmadi et al., 2015; Bobbert et al., 2017). Analytical solutions were also developed that relate the shape of the unit cell and its dimensions with the equivalent mechanical properties (Campoli et al., 2013; Ahmadi et al., 2015; Hedayati et al., 2016a, 2017; Zadpoor and Hedayati, 2016).

A possible strategy that can be adopted to design bone tissue scaffolds according to specific requirements, consists in implementing the trial and error approach, where a given scaffold design is changed, based on the outcome of *in vitro* or *in vivo* experiments, so many times, until the prescribed requirements are satisfied. However, such an approach requires costly protocols and time-consuming experiments, which led many researchers to develop computational mechanobiological models that can guide the scaffold design process. The load transfer from the scaffold to cells regulates cellular processes such as proliferation, differentiation, cellular alignment and synthesis and remodeling of extracellular matrix (Sears et al., 2012). Many studies that are available in the literature utilized computational models to investigate the role of biophysical stimuli in regulating tissue differentiation in scaffolds for bone tissue engineering (Sandino et al., 2008; Olivares et al., 2009; Boccaccio, Ballini, et al., 2011; Hendrikson et al., 2014; Velasco et al., 2015).

Numerical optimization algorithms were recently implemented to determine the best scaffold geometry, that are based on the definition of different objective functions (Dias et al., 2014; Wieding et al., 2014; Coelho et al., 2015; Roohani-Esfahani et al., 2016). In previous studies, a mechanobiology-driven optimization algorithm was proposed by some of the present authors, to determine the best geometry of scaffolds with a very simple hexahedron unit cell and with both, regular (Boccaccio, Uva, Fiorentino, Lamberti, et al., 2016) and functionally graded (Boccaccio, Uva, Fiorentino, Mori, et al., 2016) porosity. This cell was obtained starting from a cubic volume thus realizing three orthogonal holes as a cutting/protrusion of elliptic or rectangular contours along the three coordinate axes. In another study, the algorithm was successfully utilized to optimize the geometry of scaffolds based on a much more sophisticated unit cell such as the rhombicuboctahedron one (Boccaccio, Fiorentino, et al., 2018). In this article, we expanded the previous studies to: (i) determine the optimal geometry of scaffolds based on four different unit cell geometries, namely: truncated cuboctahedron, truncated cube, rhombic dodecahedron and diamond; (ii) compare the performance, - expressed in terms of percentage of the scaffold volume occupied by bone -, of all the different unit cells so far investigated for each of the seven hypothesized values of compression load. Indeed, data on the mechanical behaviour of porous structures made from the hypothesized four unit cell configurations are limited (Ahmadi et al., 2015). The model proposed can guide the orthopedic surgeon in the choice of the best scaffold to implant in a patient-specific anatomic region as well as providing useful information to the scaffold designers regarding the geometrical constraints and the amount of material needed to build the construct.

2. Materials and Methods

2.1. Modeling of the different unit cell geometries and the scaffold-granulation tissue system

Poroelastic finite element models of scaffolds were generated including four different unit cells, namely: truncated cuboctahedron, truncated cube, rhombic dodecahedron and diamond. The parametric modelling of the different cells was performed writing python scripts that were given in input to ABAQUS® version 6.12 (Dassault Systèmes, France). The beam elements included in each unit cell were hypothesized to possess both, a circular and a square cross section. Different steps were followed to assemble the four unit cells. First, a bi-dimensional trajectory was defined; second, the sweep of the cross section along the trajectory was performed; third, exploiting the symmetry of the unit cells, the solids generated by sweep were replicated using CAD tools available in ABAQUS® such as: mirror, translate, rotate, etc; finally, the unit cell so generated was cut along the faces of a cube (in which the unit cell is inscribed) so as to make the unit cell replicable in the three directions.

Truncated cuboctahedron unit cell. An octagonal trajectory t_1 was first traced with all the sides of the same length L_1. Then, a sweep of the circular or the square cross section was performed along t_1 thus obtaining a solid sub-unit including eight beams (Fig. 1(a)). Two axes (a_{1_x} and a_{1_y}, (Fig. 1(b))) were hence defined and through rotation operations around them the original solid sub-unit was replicated five times (Fig. 1(b)). The resulting disconnected sub-units were finally connected by means of beams long L_1 (Fig. 1(c)). In order to make the obtained unit cell replicable, it was cut along the planes π_{M1}, π_{M2}, …π_{M6} that delimitate a cubic volume with the side long Q (see Figs. 1(d) and 1 (e) which show the unit cells obtained after the cutting process in the case of circular and square cross section, respectively). The relationship that exists between Q and the length L_1 of the beams is given by:

$$Q = L_1 \cdot \left(1 + 4 \cdot \cos\left(\frac{\pi}{4}\right)\right) \qquad (1)$$

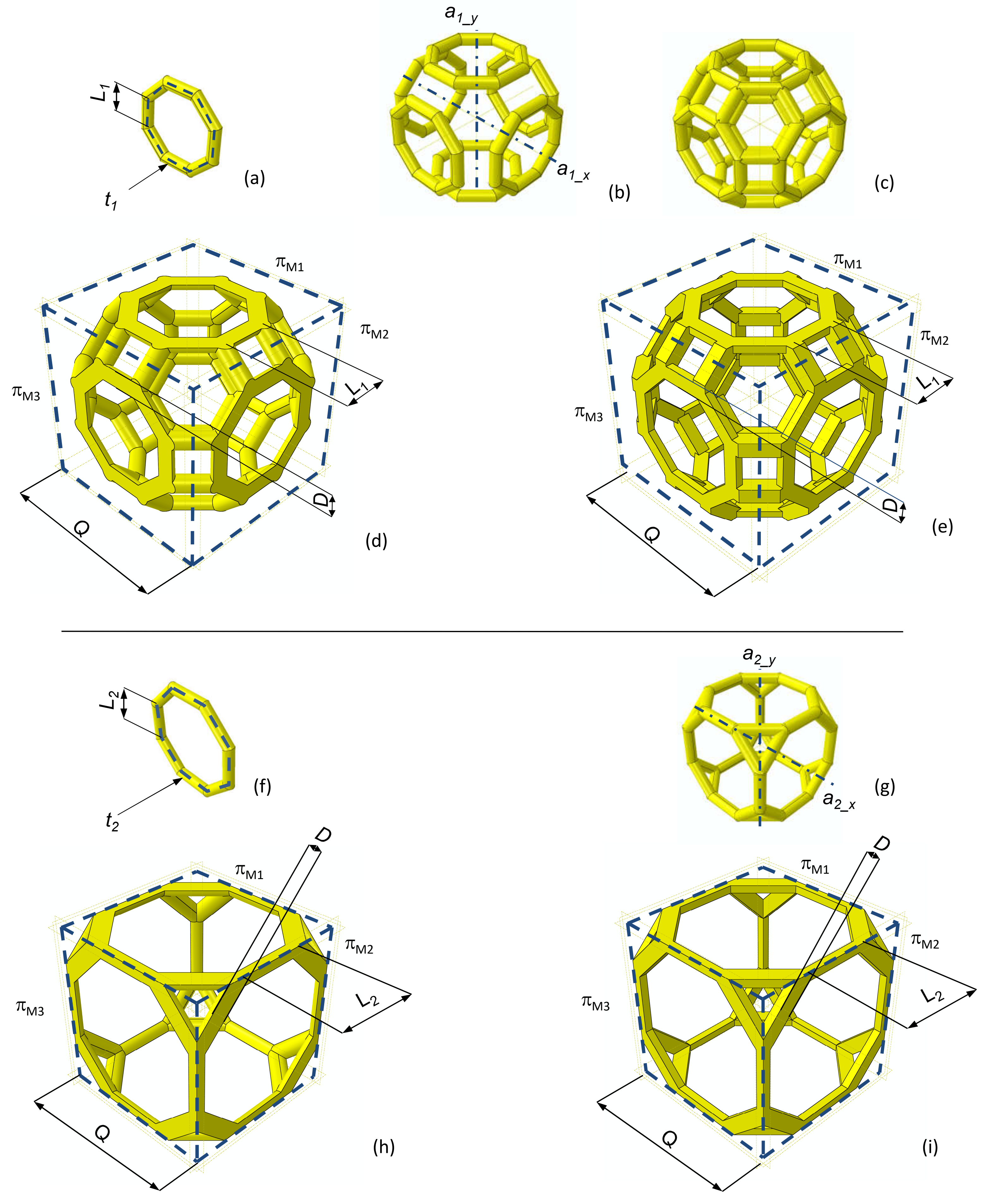

Fig. 1. Steps followed to build the truncated cuboctahedron unit cell (a-e). An octagonal trajectory t_1 was first traced. Then, a sweep of the circular or a square cross section was performed along t_1 thus obtaining a solid sub-unit including eight beams (a). Two axes (a_{1_x} and a_{1_y}) were hence defined and through rotation operations around them the original solid sub-unit was replicated five times (b). The resulting disconnected sub-units were finally connected by means of beams (c). The unit cell so generated was cut along the planes π_{M1}, π_{M2}, …π_{M6} thus obtaining the final unit cell: circular (d) and square (e) cross section. Steps followed to build the truncated cube unit cell (f-i). After building the first solid sub-unit (f), two axes were defined (a_{2_x} and a_{2_y}, (g)) and replications of the original sub-unit were performed by rotating it around a_{2_x} and a_{2_y}. The unit cell so obtained was cut along the same planes π_{M1}, π_{M2}, …π_{M6} delimiting the cubic volume $Q\times Q\times Q$ ((h) circular cross section, (i) square cross section).

For all the unit cells investigated, the dimension Q of the cube side delimiting the unit cell was kept constant and fixed equal to 637 μm, which is the same unit cell dimension hypothesized by Byrne et al. (Byrne et al., 2007). In detail, Byrne et al., proposed a fully three-dimensional approach for computer simulation of tissue differentiation and bone regeneration in a regular scaffold as a function of porosity, Young's modulus, and dissolution rate. They built a cubic scaffold model with a volume of about 7 mm^3 and including 3×3×3=27 unit cells (i.e. 3 unit cells along each side); therefore, the dimension of the single unit cell can be computed as $\frac{1}{3}\sqrt[3]{(7\cdot 10^9)\mu\text{m}^3} = 637.6\ \mu\text{m}$.

Truncated cube unit cell. After building the first solid sub-unit (Fig. 1(f)), two axes were defined (a_{2_x} and a_{2_y}, (Fig. 1(g)) and replications of the original sub-unit were performed by rotating it around a_{2_x} and a_{2_y} (Fig. 1(g)). The unit cell so obtained was cut along the same planes π_{M1}, π_{M2}, …π_{M6} delimiting the cubic volume Q×Q×Q (Fig. 1(h), circular cross section, Fig. 1(i), square cross section),. The relationship existing between Q and L_2, i.e. the length of the beams of the truncated cube unit cell, is given by:

$$Q = L_2 \cdot \left(1 + 2 \cdot \cos\left(\frac{\pi}{4}\right)\right) \qquad (2)$$

Rhombic dodecahedron unit cell. A rhombic trajectory t_3 was first traced (Fig. 2(a)). Following the hypotheses that: (1) all the beams included in the unit cell have the same length L_3, (2) the resulting unit cell is inscribable in a cubic volume, the following relationship must be satisfied for the acute angle α included in t_3 (Fig. 2(a)):

$$4 \cdot L_3 \cdot \sin\left(\frac{\alpha}{2}\right) = 2 \cdot L_3 \cdot \cos\left(\frac{\alpha}{2}\right) \leftrightarrow \tan\left(\frac{\alpha}{2}\right) = \frac{1}{2} \rightarrow \alpha = 53.13° \qquad (3)$$

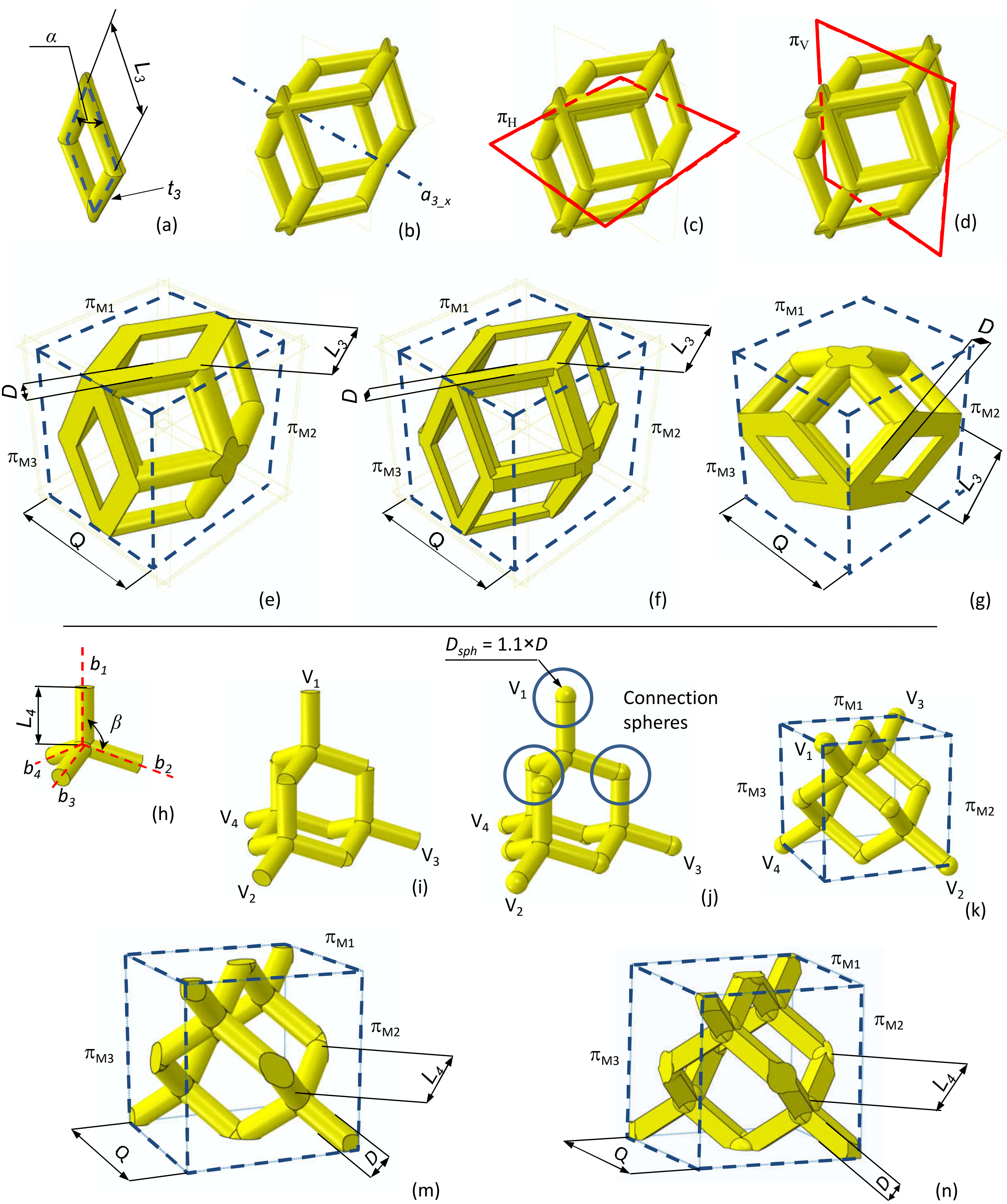

Fig. 2. Steps followed to build the rhombic dodecahedron unit cell (a-g).A rhombic trajectory t_3 was first traced and the sweep of a circular or a square section was then performed (a) thus obtaining a first solid sub-unit. After defining the axis a_{3_x} (b), three replications of the initial sub-unit were obtained by rotating it around a_{3_x} by the angles π/2, π and 3π/2. To link completely the cell, half sub-units were finally added that lie in the horizontal plane π_H (c) and in the vertical plane π_V (d). The resulting unit cell was finally cut along the faces of the planes π_{M1}, π_{M2}, …π_{M6} ((e) circular cross section, (f) square cross section). In order to evaluate the effect of the cell orientation, the same rhombic topology with a rotation of π/2 was modelled (g). Steps followed to build the diamond unit cell (h-n). This unit cell was built by performing the protusion of the cross section along linear paths (h) inclined one each other by the angle β = 109.47°. In order to guarantee the continuity (i) between the single beams connections spheres were included in the model (j). Once the unit cell was built, it was properly oriented to have the vertices V_1, V_2, V_3 and V_4 coincident with those of the cubic volume Q×Q×Q (k). Cuts were finally performed along the faces of the planes π_{M1}, π_{M2}, …π_{M6} ((m) circular cross section, (n) square cross section).

The sweep of a circular or a square section was then performed (Fig. 2(a)) thus obtaining a first solid sub-unit. After defining the axis a_{3_x} (Fig. 2(b)), three replications of the initial sub-unit were obtained by rotating it around a_{3_x} by the angles π/2, π and 3π/2. To link completely the cell, half sub-units were finally added that lie in the horizontal plane π_H (Fig. 2(c)) and in the vertical plane π_V (Fig. 2(d)). The resulting unit cell was finally cut along the faces of the planes π_{M1}, π_{M2}, …π_{M6} delimiting the cubic volume $Q \times Q \times Q$ (Fig. 2(e), circular cross section, Fig. 2(f), square cross section). In this case, the relationship between Q and L_3 assumes the form:

$$Q = 4 \cdot L_3 \cdot \sin\left(\frac{\alpha}{2}\right) \qquad (4)$$

In order to evaluate the effect of the cell orientation, the same rhombic topology with a rotation of π/2 was also modelled (Fig. 2(g)).

Diamond unit cell. L_4 long beams were built and oriented according to axes (denoted as b_1, b_2, b_3 and b_4 (Fig. 2(h)) mutually inclined by the angle β = 109.47° (Ahmadi et al., 2014). In order to guarantee the continuity (Fig. 2(i)) between the single beams, connections spheres were included in the model with a diameter 10% larger than that of the beams (Fig. 2(j)). Once the unit cell was built, it was properly oriented to have the vertices V_1, V_2, V_3 and V_4 coincident with those of the cubic volume $Q \times Q \times Q$ (Fig. 2(k)). Cuts were finally performed along the faces of the planes π_{M1}, π_{M2}, …π_{M6} (Fig. 2(m), circular cross section, Fig. 2(n) square cross section). The relationship between Q and L_4, i.e. the length of the beams, is reported below:

$$Q \cdot \sqrt{2} = 4 \cdot L_4 \cdot \sin\left(\frac{\beta}{2}\right) \qquad (5)$$

The specific values of length of the beams (i.e. L_1, L_2, L_3 and L_4) utilized in the different unit cells are listed in Table 1.

Table 1. Length of the beams included in unit cells investigated.

Unit cell	Beam length L_i (i=1, 2, ...4) [μm]	Unit cell dimension Q [μm]
Truncated Cuboctahedron	$L_1 = 166.39$	$Q = 637$
Truncated Cube	$L_2 = 263.85$	
Rhombic Dodecahedron	$L_3 = 356.09$	
Diamond	$L_4 = 275.83$	

The unit cells so generated were replicated by properly mirroring them with respect to the planes π_{M1}, π_{M2}, …π_{M6}. The resulting scaffold model has cubic shape with the side long $h = 4 \times Q = 2548$ μm, which is consistent with the dimensions utilized by Byrne et al. (Byrne et al., 2007) (Fig. 3(a)).

The scaffold pores were hypothesized, according to previous studies (Boccaccio, Uva, Fiorentino, Lamberti, et al., 2016; Boccaccio, Uva, Fiorentino, Mori, et al., 2016), to be occupied by granulation tissue. The model of the granulation tissue (highlighted in red, Fig. 3(a)) was obtained with the Boolean operation of subtraction from the volume $h \times h \times h$, the volume occupied by the scaffold. A tie constraint was established between the surfaces of the scaffold and those adjacent of the granulation tissue while a rigid plate was fixed on the top surface of the model (Fig. 3(a)) to apply a compression load F on it. In detail, F was hypothesized to assume seven different values that correspond to have, on the model upper surface a force per unit area $p = F / (h \times h)$ of: 0.05, 0.1, 0.15, 0.25, 0.5, 1.0 and 1.5 MPa.

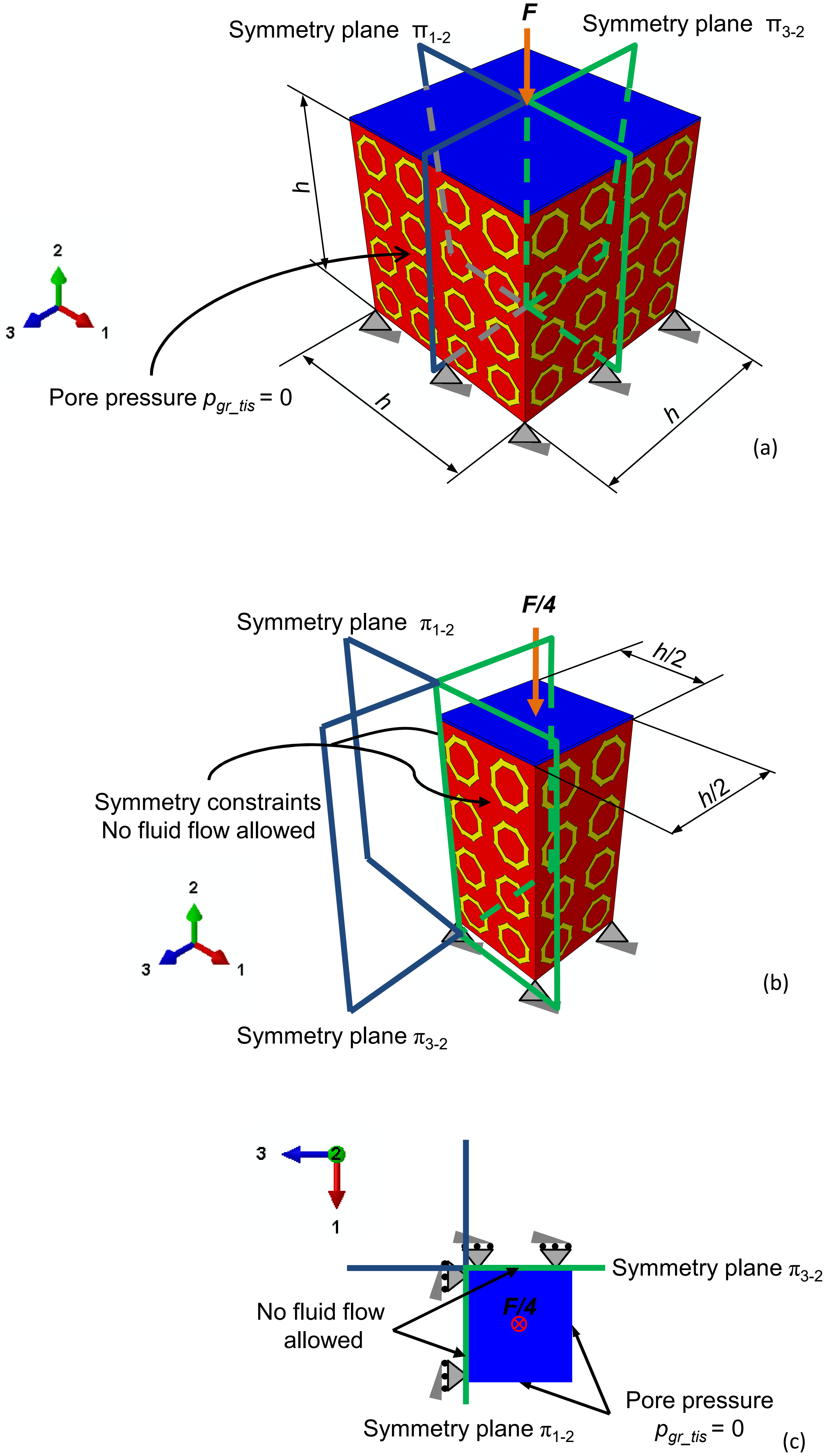

Fig. 3. Boundary and loading conditions acting on the scaffold model (a). Exploiting the symmetry of the problem, the volume analyzed was reduced to one quarter of the total volume (b). Symmetry constraints were utilized on the faces of the model lying on the symmetry planes $\pi_{1\text{-}2}$ and $\pi_{3\text{-}2}$ where the absence of any fluid flow was imposed ((b) and (c)).

These force values, that are consistent with those hypothesized by Byrne et al. (Byrne et al., 2007), correspond to medium-low loads acting on the spongy bone that exhibits, depending on its apparent density, an ultimate compressive strength of 10-20 MPa (Keaveny and Hayes, 1993). Between the plate and the top surface of the model (which includes the scaffold and the granulation tissue) constraint equations were established that impose that the vertical displacements (i.e. along the direction 2, Fig. 3(a)) of the plate are equal to those of the scaffold/granulation tissue system. The load F was ramped, according to a previous study (Boccaccio, Kelly, et al., 2011) over a time interval of 1 second. The bottom surface of the model was clamped thus fixing all the degrees of freedom. According to Byrne et al. (Byrne et al., 2007), following the hypothesis that the surrounding tissue does not prevent the fluid from escaping, a pore pressure p_{gr_tis} equal to zero was applied on the outer surfaces of the granulation tissue to simulate the condition of free exudation of fluid (Fig. 3(a)).

Both scaffold and granulation tissue were modelled as poroelastic materials and the material properties implemented are the same as those utilized in previous studies (Boccaccio, Uva, Fiorentino, Lamberti, et al., 2016; Boccaccio, Uva, Fiorentino, Mori, et al., 2016; Boccaccio, Fiorentino, et al., 2018; Boccaccio, Uva, et al., 2018) (Table 2).

Table 2. Material properties utilized in the model of the scaffold and granulation tissue

Material Properties	Scaffold	Granulation tissue
Young's modulus [MPa]	1000	0.2
Poisson's ratio	0.3	0.167
Permeability [m^4/N/s]	1×10^{-14}	1×10^{-14}
Porosity	0.5	0.8
Bulk modulus grain [MPa]	13920	2300
Bulk modulus fluid [MPa]	2300	2300

Exploiting the symmetry of the problem, the volume analyzed was reduced to one quarter of the total volume (Fig. 3(b)). Symmetry constraints were utilized on the faces of the model lying on the symmetry planes π_{1-2} and π_{3-2}. No fluid was allowed to flow across the symmetry planes; any fluid flow through these planes, indeed, would imply the loosing of the symmetry condition (Figs. 3(b) and 3(c)).

Tetrahedral four-node, linear displacement and pore pressure elements (C3D4P) available in ABAQUS® were utilized to mesh the model of both, the scaffold and the granulation tissue (Fig. 4). Setting an average element size of 20 µm and a maximum deviation factor for the curvature control of 0.01, the entire model (regardless of the specific unit cell considered) included about 5 million elements with 1 million nodes. Nonlinear finite element analyses were run to take into account the geometric nonlinearities.

It is worthy to note that for a given unit cell, all the beams (included in the unit cell) were hypothesized to possess the same cross section dimension *D* (Figs. 1 and 2). In detail, in the case of the circular cross section, *D* represents the diameter of the section (Figs. 1 and 2) while in the case of the square cross section, *D* is the side length of the square (Figs. 1 and 2). The value of *D* was determined, for each of the hypothesized loads and for each unit cell geometries, via the optimization algorithm described below.

2.2. Mechanobiological approach

After the scaffold implantation, mesenchymal stem cells invade it thus triggering all the phenomena involved in the healing process of the bony tissue. According to a previous study (Boccaccio, Uva, Fiorentino, Lamberti, et al., 2016), the granulation tissue was hypothesized to be uniformly occupied by mesenchymal stem cells (MSCs). After dispersal,

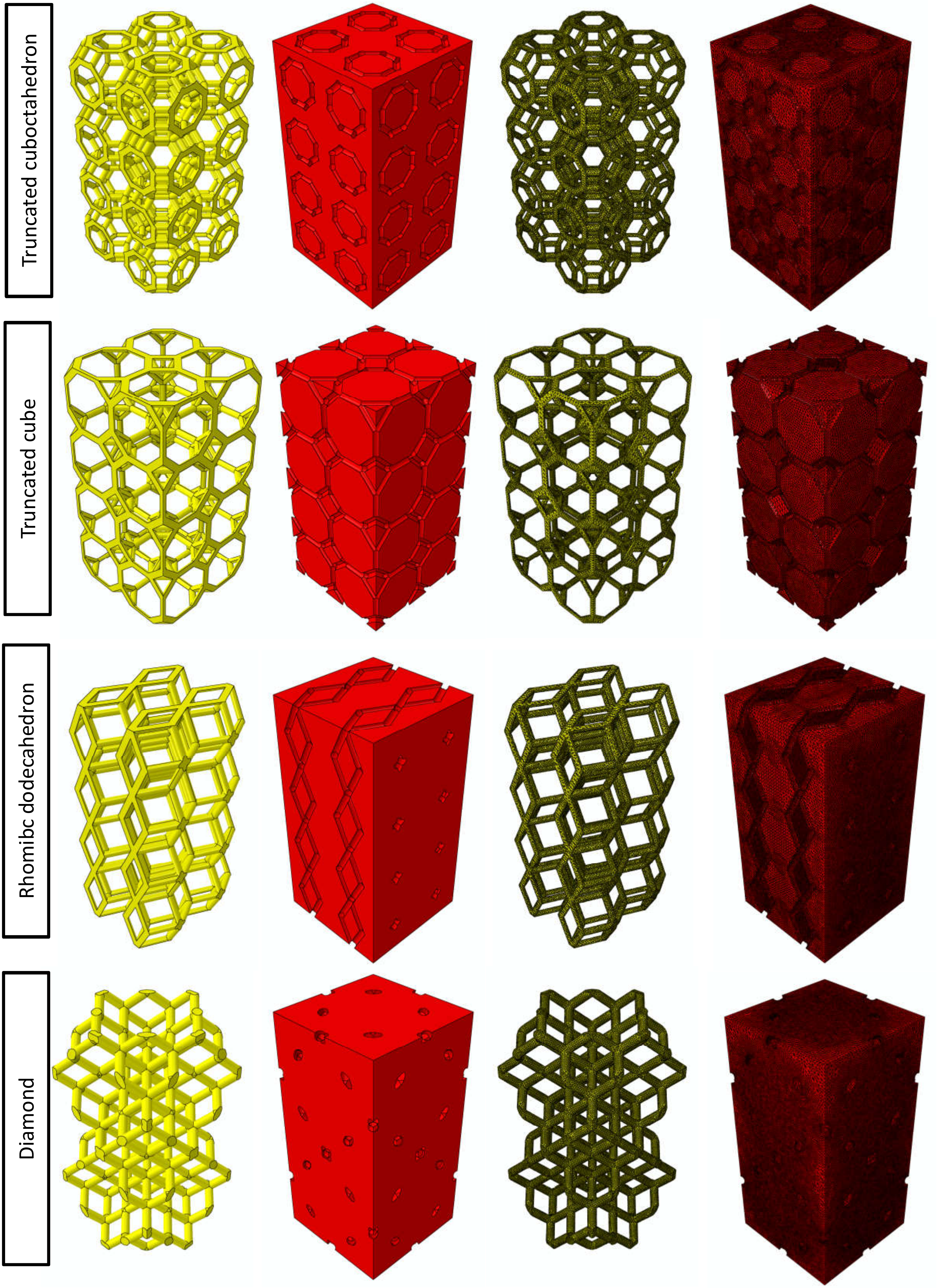

Fig. 4. Scaffold and granulation tissue models (first two columns) and finite element mesh utilized (second two columns).

MSCs start to differentiate based on the values of a biophysical stimulus *S*, which is a function of the octahedral shear strain γ (and hence the principal strains) and the interstitial fluid flow ν (Prendergast et al., 1997) according to the following relationship:

$$S = \frac{\gamma}{a} + \frac{\nu}{b} \qquad (6)$$

a and *b* are empirical constants, which have values of 3.75 % and 3 μm/s, respectively (Huiskes et al., 1997). MSCs can differentiate towards different tissue phenotypes according to the following inequalities:

$$\begin{cases} S > 3 \rightarrow Fibroblasts\ (Fibrous\ tissue) \\ 1 < S < 3 \rightarrow Chondrocytes\ (Cartilage\ tissue) \\ 0.53 < S < 1 \rightarrow Osteoblasts\ (Immature\ bone\ tissue) \\ 0.01 < S < 0.53 \rightarrow Osteoblasts\ (Mature\ bone\ tissue) \\ 0 < S < 0.01 \rightarrow Bone\ resorption \end{cases} \qquad (7)$$

2.3. Optimization algorithm

To find the optimal dimension *D* of the beam cross section, an *ad hoc* algorithm was written in Matlab environment. To run the algorithm, the user is first asked to select the unit cell (Step [1], Fig. 5), the shape of the cross section (Step [2], Fig. 5) and the value of load acting on the scaffold model (Step [3], Fig. 5). For instance, in Fig. 5 the case where, the truncated cube unit cell, the circular cross section and the load (per unit area) of *p* = 0.15 MPa are selected, is shown. Then the algorithm, after requiring to enter an initial possible value of *D* (Step [4], Fig. 5), writes a python script (Step [5], Fig. 5) corresponding just to the selected options. The script is given in input to ABAQUS, which builds the CAD model,

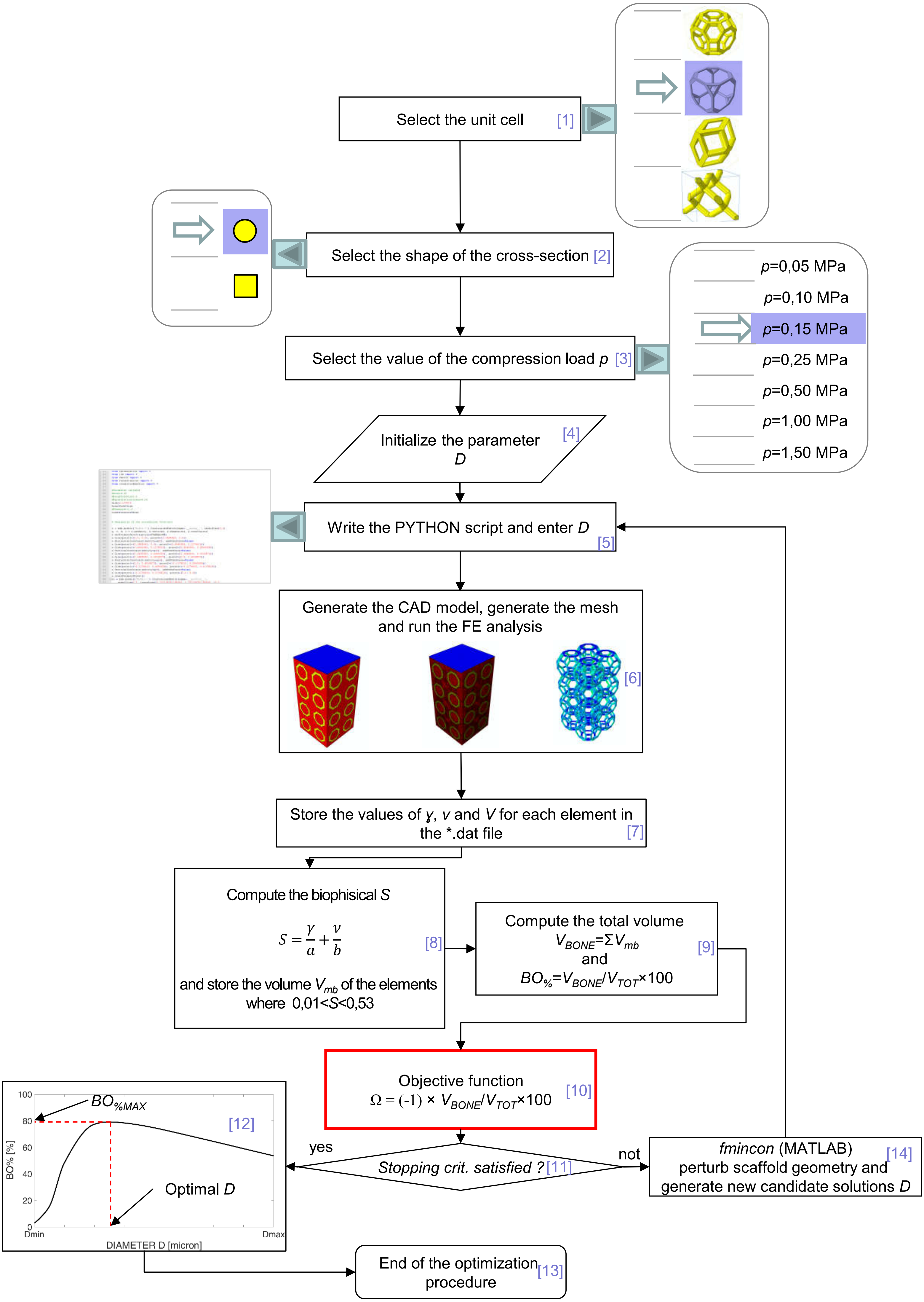

Fig. 5. Schematic of the algorithm written in Matlab environment to determine the optimal dimension D for different unit cell geometries.

generates the finite element mesh, applies the boundary and loading conditions and runs the FE analysis (Step [6], Fig. 5). All the beams included in the scaffold based on the selected unit cell, possess the same diameter D entered by the user. Once the FE analysis terminates, the algorithm stores, for each element of the granulation tissue domain, the interstitial fluid flow v, the octahedral shear strain γ and the volume V (Step [7], Fig. 5). Then, (for all the elements included in the granulation tissue model) the biophysical stimulus S is computed according to the equation (6) and compared with the numerical values reported in the inequalities (7) (Step [8], Fig. 5). For the elements where the formation of mature bone is predicted (i.e. the inequality $0.01 < S < 0.53$ is satisfied), the volume $V = V_{mb}$ is stored in another array. The total volume of the scaffold model occupied by bone V_{BONE} is then computed as the sum of the volumes V_{mb}, while the percentage of the scaffold volume occupied by bone $BO_{\%}$ is computed as:

$$BO_{\%} = \frac{V_{BONE}}{V_{TOT}} \cdot 100 \qquad (8)$$

where $V_{TOT} = h \cdot \frac{h}{2} \cdot \frac{h}{2}$ is the total volume of the scaffold (Step [9], Fig. 5). The objective function that must be minimized was defined as:

$$\Omega(D) = (-1) \cdot BO_{\%} \qquad (9)$$

while the optimal value of D that minimizes Ω was computed by means of the function *fmincon* available in Matlab (Step [10], Fig. 5). This function, designed to find the minimum of nonlinear multivariable functions, requires the user to specify proper stopping criteria. It perturbs the scaffold geometry, i.e. changes the value of D, until the minimum value of Ω, i.e. the maximum value of $BO_{\%}$, is identified. Once the stopping criteria are satisfied and hence the minimum value of Ω found, the algorithm stops giving in output the curve of $BO_{\%}$ in function of the different values of *D* tested during the optimization cycle. In other words, for each value of *D* utilized as candidate solution for the optimization problem (9), the algorithm stores the corresponding value of $BO_{\%}$. Once the minimum value of Ω is found, the algorithm shows in a diagram the amounts $BO_{\%}$ in function of the corresponding values of *D* for which they were computed. The optimal value of *D* will be the one where $BO_{\%}$ reaches its maximum value $BO_{\%MAX}$ (Fig. 5, Steps [12] and [13]). Conversely, if the stopping criteria are not met, *fmincon* generates other candidate solutions *D* that are entered in the python script thus commencing a new iteration cycle (Fig. 5, Steps [14]). For each candidate solutions *D*, a scaffold model including all the beams with diameter *D* is built and submitted to finite element analysis.

The lower (D_{min}) and upper (D_{max}) bounds between which the candidate solutions were chosen are listed, for each of the unit cells investigated, in Table 3.

Table 3. Lower and upper bounds utilized in the optimization algorithm for the different unit cell geometries.

Unit Cell	D_{max_i} (i=1, 2…4) [μm]	$D_{max\_i,}$ (i=1, 2…4) [μm]	D_{min} [μm]
	Circular cross section	Square cross section	Circular or square cross section
Truncated Cuboctahedron	D_{max_1} = 166.39	D_{max_1} = 117.66	28
Truncated Cube	D_{max_2} = 152.33	D_{max_2} = 109.29	
Rhombic Dodecahedron	D_{max_3} = 284.87	D_{max_3} = 284.87	
Diamond	D_{max_4} = 260.01	D_{max_4} = 183.88	

The lower bound was fixed equal to D_{min} = 28 μm as, for the hypothesized levels of load, values of D smaller than this number are not of interest. Different values were instead given to the upper bound (D_{max}) depending on the unit cell type. The values of D_{max} were fixed based on the hypothesis that the scaffold connectivity (i.e. the number of holes present in the scaffold) must remain constant for every value of D utilized as candidate solution. In other words, we imposed that the number of holes present in the scaffold must be the same for all the values of $D \in [D_{min}; D_{max}]$. The geometrical formulations utilized to determine D_{max} for all the unit cells are reported in the Appendix A.

Each analysis had a duration of approximately 1.5 hour. Considering that: (i) four unit cells were investigated; (ii) seven loading cases were hypothesized; (iii) two different cross sections were studied, for each unit cell; (iv) each optimization analysis required at least 30 analyses to correctly identify the minimum of Ω; other 14 optimization analyses were run for the rotated rhombic dodecahedron unit cell (see Results and Discussion, section 3.5), it follows that a total of: $4 \times 7 \times 2 \times 30 + 14 \times 30 = 2100$ analyses were run which took, approximately, 3150 hours of computation.

3. Results and Discussion

3.1. Truncated cuboctahedron

Increasing dimensions of the optimal diameter D were predicted for increasing levels of load (Figs. 6(a) and (b)). This is consistent with our expectations. In fact, as the load increases, the resulting scaffold deformation increases too (if D remains constant), which

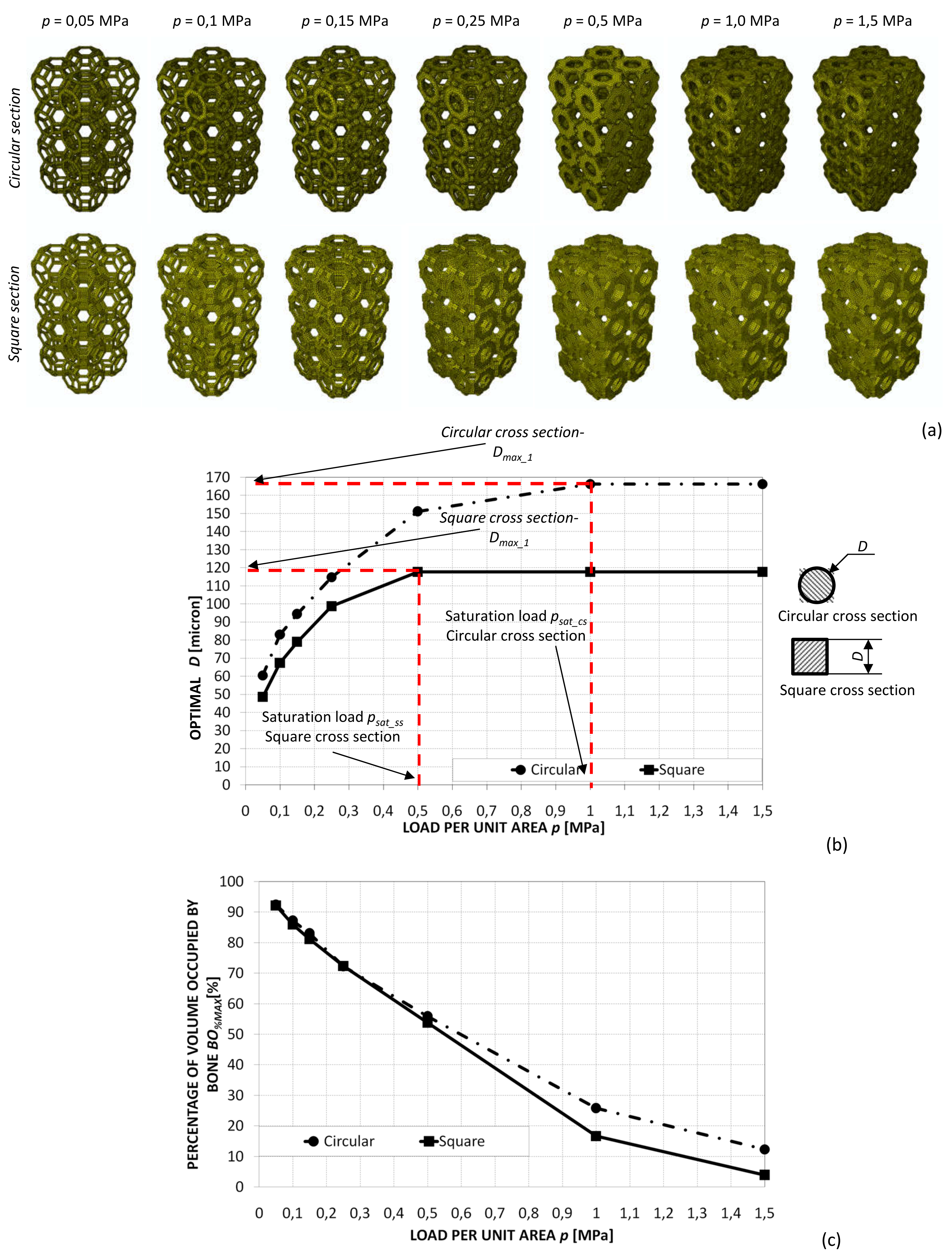

Fig. 6. Optimization of the truncated cuboctahedron unit cell. (a) Optimal scaffold geometries predicted for circular (top) and square (bottom) cross section. Values of the optimal diameter D (b) and of $BO_{\%MAX}$ (c) predicted for different levels of load.

leads, according to Eqs. (6) and (7), to the formation of soft tissues such as fibrous tissue and/or cartilage. To contrast the excessive deformation, the algorithm increases the dimension D, thus making the scaffold stiffer and promoting the formation of bone. However, the trend of the optimal D in function of the load is asymptotic (Fig. 6(b)). Due to the constraints imposed to the upper bound D_{max_1}, the unlimited increase of the cross section is not allowed and consequently, a saturation load exists behind which the optimal D cannot increase anymore but must be $D = D_{max\_1}$. Interestingly, the amounts of bone $BO_{\%MAX}$ predicted for the circular and square cross sections are very close for low load levels but differ significantly for higher values of p (Fig. 6(c)). This behavior can be justified with the argument that for the square cross section the saturation load (p_{sat_ss} = 0.5 MPa) is smaller than that predicted for the circular cross section (p_{sat_cs} = 1 MPa). In other words, for the square cross section the range of the load values p where the algorithm can properly optimize the cross section dimension D is smaller than the case of the circular cross section. Consequently, for load levels higher than the saturation load, the amounts of bone $BO_{\%MAX}$ predicted for the square cross sections are smaller than those obtained for the circular one.

3.2. Truncated cube

Also in this case, the optimal diameter D was predicted to increase for increasing levels of the applied compression load p (Fig. 7(b)). However, for the truncated cube unit cell, the saturation load was smaller than that predicted for the truncated cuboctahedron and for both, square and circular cross section, assumed the value of $p_{sat\_ss} = p_{sat\_cs}$ = 0.25 MPa (Fig. 7(b)). In other words, for values of p higher than the saturation load, the optimization algorithm

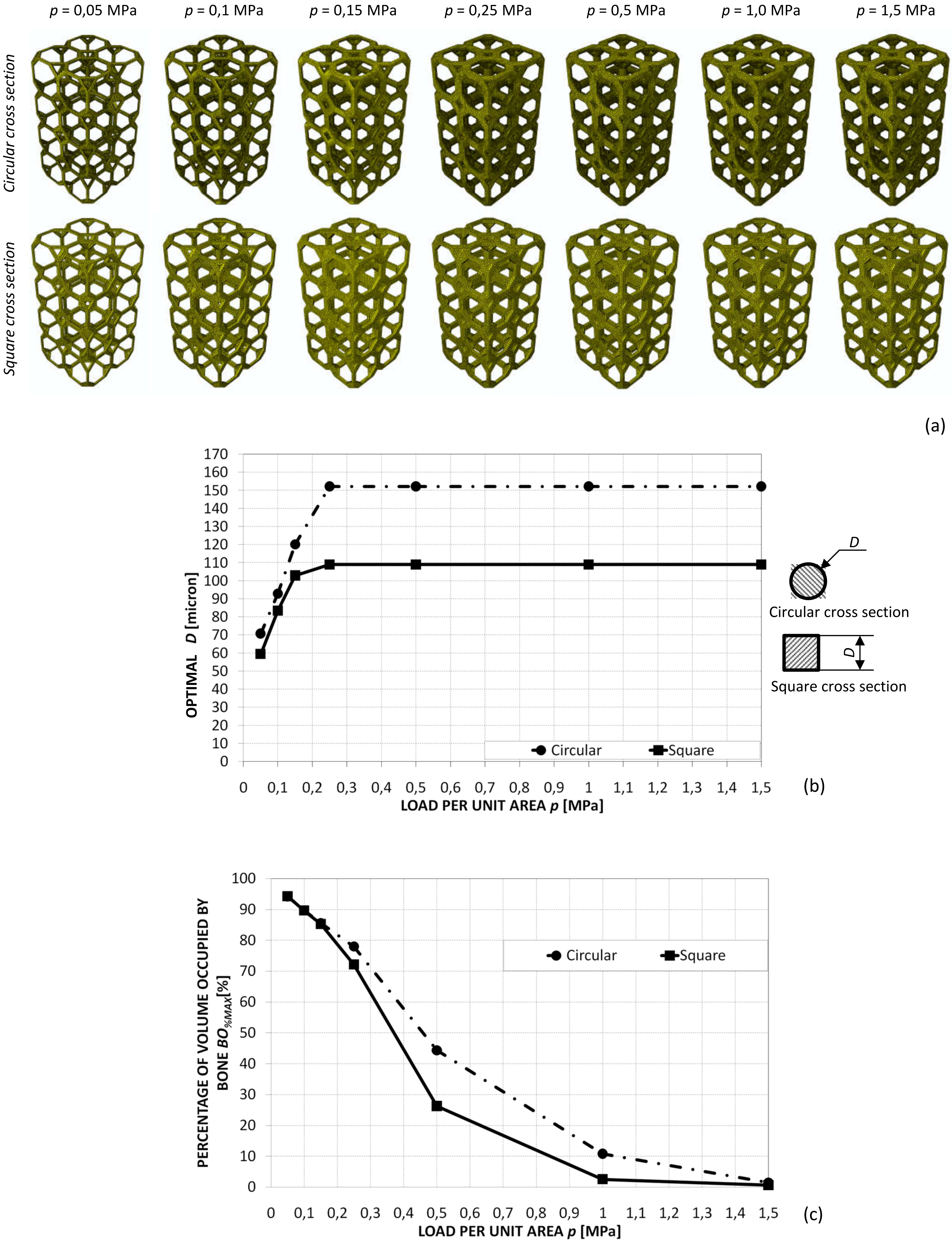

Fig. 7. Optimization of the truncated cube unit cell. (a) Optimal scaffold geometries predicted for circular (top) and square (bottom) cross section. Values of the optimal diameter D (b) and of $BO_{\%MAX}$ (c) predicted for different levels of load.

gives in output always the same scaffold geometry (Fig. 7(a)). The amounts of bone $BO_{\%MAX}$ predicted for the circular cross section were overlappable to those predicted for the square cross section for load values within the intervals $0.05 < p < 0.15$ MPa and $p > 1.5$ MPa while differed significantly within the interval $0.15 < p < 1.5$ MPa (Fig 7(c)). In particular, for p = 1.5 MPa, very small amounts (≈ 1 %) of bone $BO_{\%MAX}$ were predicted to form.

3.3. Rhombic dodecahedron

The trend of the optimal value of D in function of the load p, is increasing but does not present, as in the previously analyzed cases, an asymptote. In other words, within the load levels hypothesized in this study, the saturation condition is never met (Fig. 8(b)) and hence the optimizer, for all the values of p, can identify the optimal scaffold geometry (Fig. 8(a)). The amounts of bone predicted for the square cross section were practically overlapped to those computed for the circular one (Fig. 8(c)).

3.4. Effect of the unit cell orientation

A peculiar aspect of the rhombic dodecahedron unit cell is that it can be oriented, with respect to the loading direction, in two different ways: orientation A (which is the orientation previously described (Fig. 8)) and orientation B, where the longer diagonal of the rhombic elements is parallel and perpendicular, respectively, to the loading direction (Fig. 9(a)).

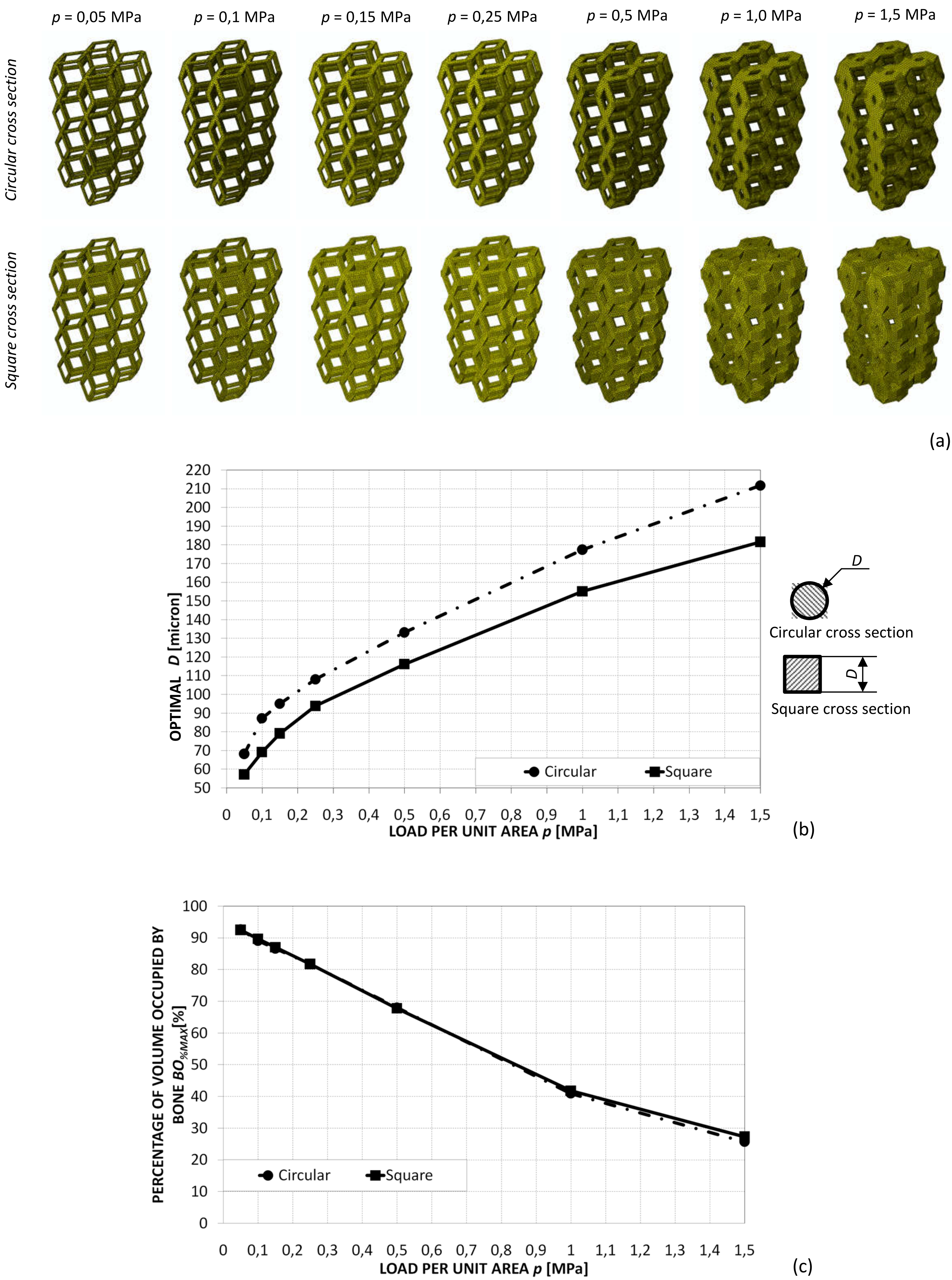

Fig. 8. Optimization of the rhombic dodecahedron unit cell. (a) Optimal scaffold geometries predicted for circular (top) and square (bottom) cross section. Values of the optimal diameter D (b) and of $BO_{\%MAX}$ (c) predicted for different levels of load.

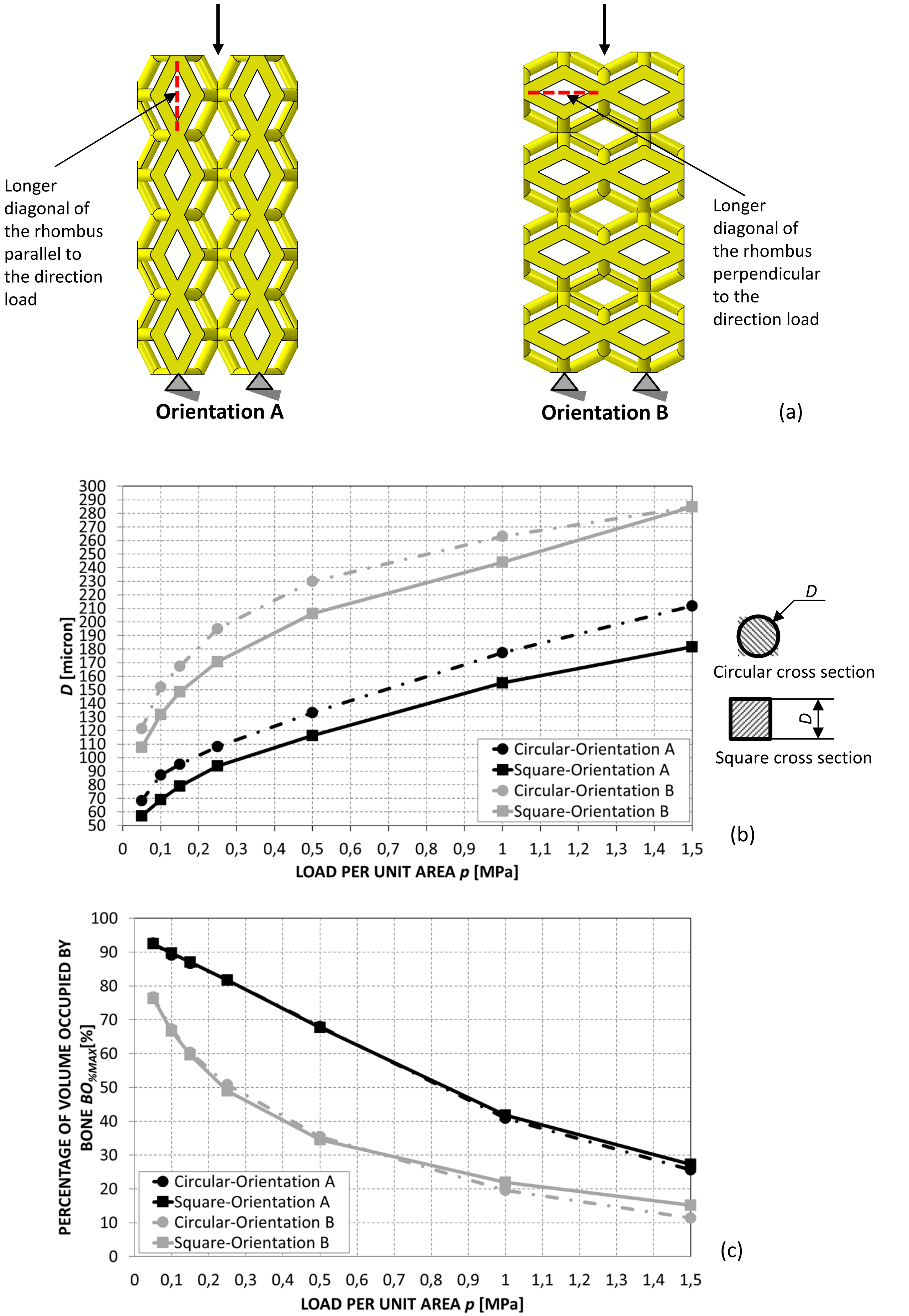

Fig. 9. Comparison between two different unit cell orientations: Orientation A and Orientation B (a). Values of the optimal diameter D (b) and $BO_{\%MAX}$ (c) predicted by the algorithm for different levels of load and for the two different cell orientations.

Interestingly, for orientation B, the optimal dimensions *D* are significantly larger than those computed for orientation A (Fig. 9(b)). This result can be explained with the argument that with orientation A the beams can better distribute/transfer -compared to orientation B- the load within the scaffold construct, and hence the optimization algorithm can predict rather small values of *D*. Conversely, in the case of orientation B the spatial arrangement of beams is less favorable and therefore the algorithm tends to balance this disadvantage by increasing the dimension *D*. Given that for orientation B the optimal diameters *D* are larger and hence a larger volume of the scaffold system is occupied by beams, it follows that a smaller volume is available for bone, which explains why for this orientation smaller amounts of bone $BO_{\%MAX}$ were predicted (Fig. 9(c)). Interestingly, no important differences were observed between $BO_{\%MAX}$ values computed for the circular cross section and those computed for the square one.

3.5. Diamond

Circular and square cross sections showed a different behavior (Figs. 10(a) and (b)). In fact, while the square cross section presented a saturation point at p = 1 MPa, for the circular one no saturation load was found within the investigated load interval. The values of $BO_{\%MAX}$ were very close for low levels of p and started to diverge as the square cross section reached the saturation point (Fig. 10(c)). After this point, the difference became larger as the optimizer could increase further the value of *D* in the case of the circular section but could not do the same for the square cross section.

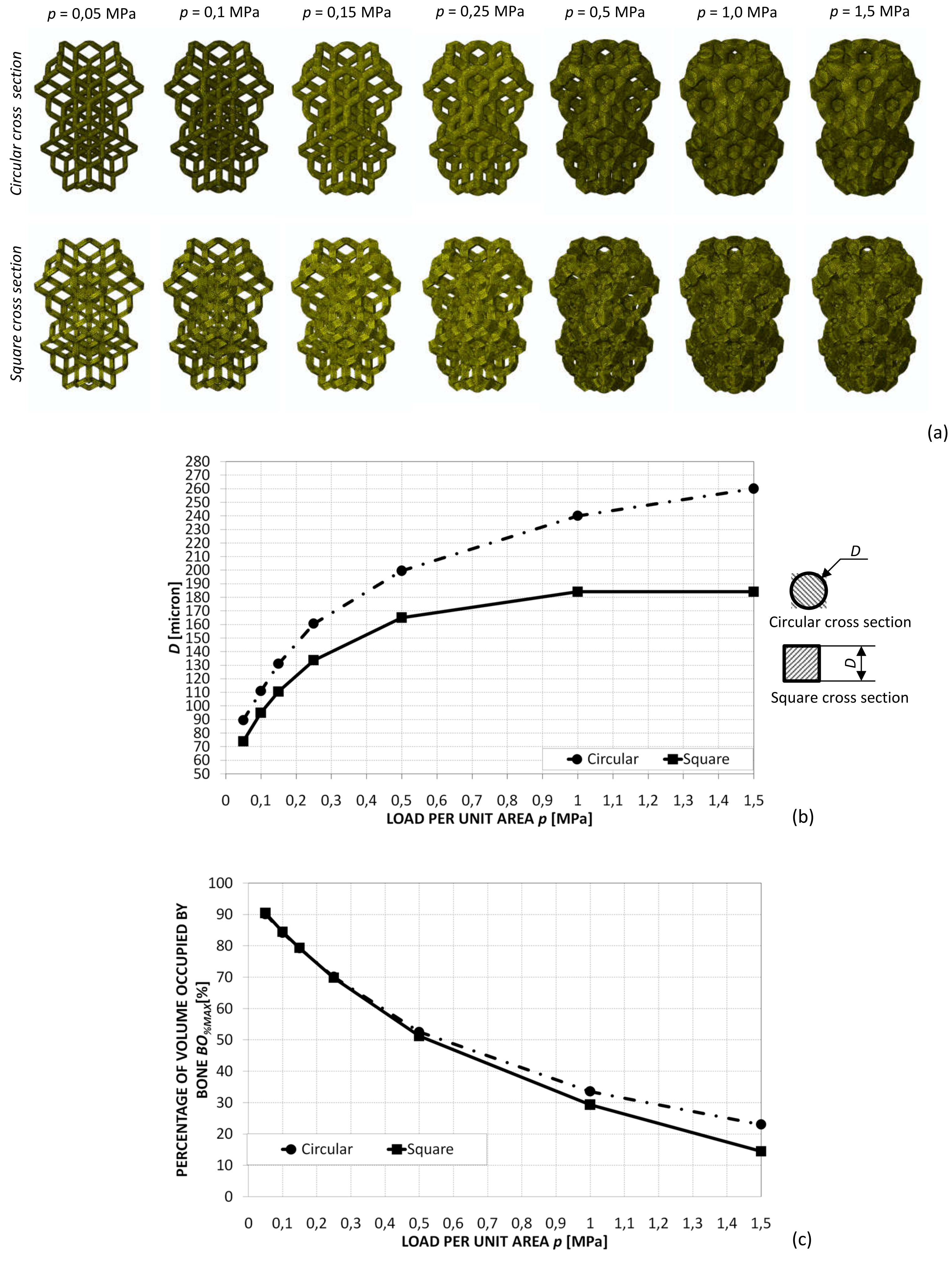

Fig. 10. Optimization of the diamond unit cell. (a) Optimal scaffold geometries predicted for circular (top) and square (bottom) cross section. Values of the optimal diameter D (b) and of $BO_{\%MAX}$ (c) predicted for different levels of load.

3.6. Comparison of different unit cells

The amounts of bone predicted by the proposed optimization algorithm for the different unit cells investigated were compared with those obtained in previous studies investigating other unit cells, namely, a rhombicuboctahedron (Boccaccio, Fiorentino, et al., 2018) unit cell including beams with both circular and square cross section and an hexahedron unit cell with both elliptic and rectangular pores (Boccaccio, Uva, Fiorentino, Lamberti, et al., 2016) (Fig. 11(a)). In particular, $BO_{\%MAX}$ predicted for all the investigated unit cells in the case of circular cross section were compared with those obtained for rhombicuboctahedron with circular cross section and hexahedron with elliptic pores (Fig. 11(b)). $BO_{\%MAX}$ predicted in the case of square cross section were instead compared with those computed for rhombicuboctahedron with square cross section and hexahedron unit cell with rectangular pores (Fig. 11(c)). In the case of the circular cross section and for very low levels of load, the best unit cell was predicted to be the truncated cube. For medium-low loads, the rhombic dodecahedron produced the largest amounts of bone, while for the highest ones, the hexahedron unit cell with elliptic pores (Fig. 11(b)). A very intriguing behavior was observed for the truncated cube that was predicted to be the best unit cell for low values of p and the worst one for high levels of load (Fig. 11(b)). In the case of the square cross section and for the entire range of load investigated, the best unit cell was predicted to be the hexahedron unit cell with rectangular pores (Fig. 11(c)). In general, for low values of load, the diamond was predicted to be the worst unit cell, while for high values, the worst unit cell was the truncated cube (Fig. 11(c)). This is true in both cases, circular and square cross section.

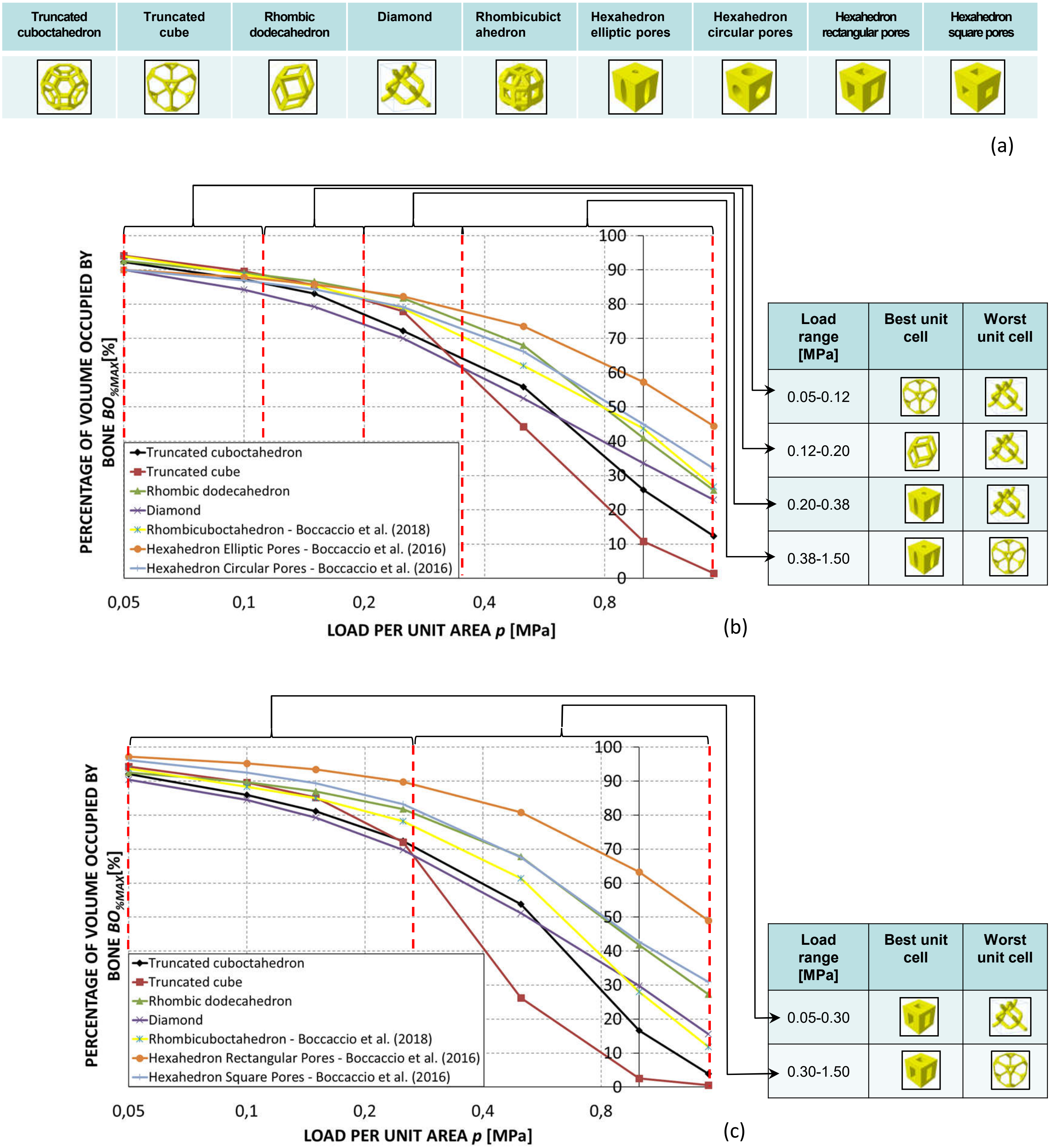

Fig. 11. Comparison of the amounts of bone predicted to form $BO_{\%MAX}$ for different unit cell geometries (a) with both circular (b) and square (c) cross section. In order to improve the visualization of data, a logarithmic scale was utilized on the axis of the load.

For all the optimized scaffolds, the percentage of the volume occupied by the mature bone (i.e. the same quantity so far denoted as $BO_{\%MAX}$), the scaffold itself and other tissues (cartilage, fibrous tissue etc) was diagrammed in function of the load (Fig. 12). For the sake of brevity, the results regarding only the circular cross section were reported. For low values of load, small percentages of volume were predicted to be occupied by other tissues but, for higher values, these percentages became significant especially for the truncated cuboctahedron (Fig. 12(a)) and the truncated cube (Fig. 12(b)) units cells. This can be explained with the saturation load that was predicted to be very low just for these unit cells. For all the load cases investigated, the smallest volume percentage occupied by scaffold was predicted for the truncated cube (Fig. 12(b)).

The present work has some limitations mainly associated to the simplifications required to carry out the study. First, a simplified and regular scaffold geometry with a cubic volume was hypothesized while in the real/clinical context scaffold geometries must follow the shape, often irregular, of the space where the bone tissue is deficient. However, the representative models utilized in this study allow to estimate with a reasonably good degree of approximation the general behavior of the different unit cell based scaffolds investigated as well as to compare their mechanobiological performance. The second limitation is that the scaffold dissolution process was not taken into account and the amounts of bone $BO_{\%}$ computed to determine the optimal scaffold geometry were those present at the early stages of the bone development process. In other words, the identification of the optimal values D was carried out on scaffold models that do not experience a temporal evolution. In reality, including temporal changes would lead to computational times tremendously longer than those spent in the present study. The third limitation is the hypothesis that the optimal scaffold geometry is just driven by mechanical stimuli. In reality, complex biochemical

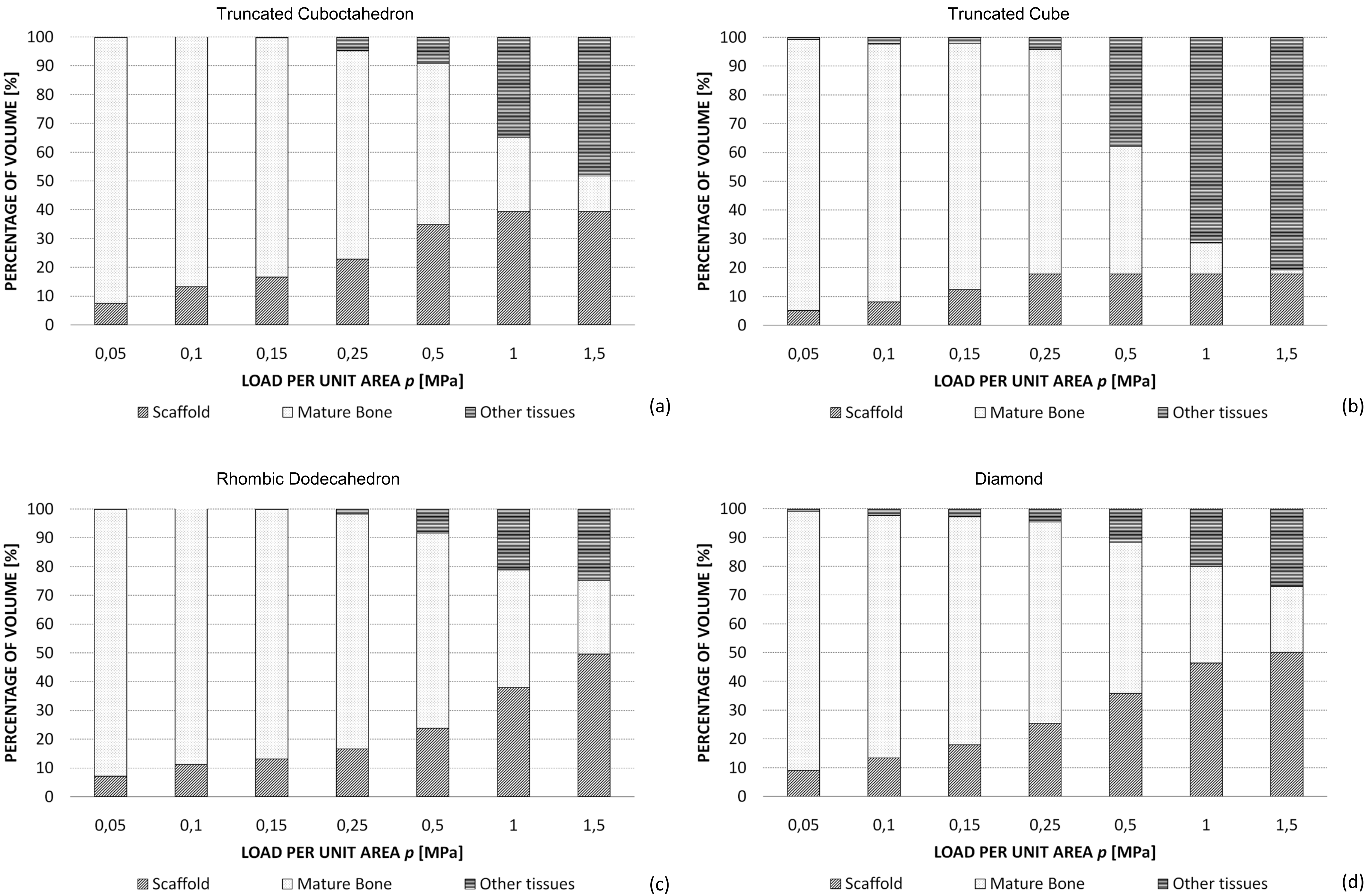

Fig. 12. Percentage of volume occupied by mature bone, scaffold and other tissues predicted for truncated cuboctahedron (a), truncated cube (b), rhombic dodecahedron (c) and diamond (d) unit cells. For the sake of brevity, the only results regarding the circular cross section are reported. Note. The percentage occupied by mature bone is the same quantity so far denoted as $BO_{\%MAX}$.

processes take place during the healing process that depend on factors such as angiogenesis (Sandino et al., 2010), oxygen, nutrients supplies and biochemical signaling (Geris et al., 2008; Corredor-Gómez et al., 2016). The fourth limitation is that the analyses carried out refer to specific scaffold material properties, i.e. those listed in Table 2, that are the same as those utilized in previous studies (Boccaccio, Uva, Fiorentino, Lamberti, et al., 2016; Boccaccio, Uva, Fiorentino, Mori, et al., 2016; Boccaccio, Uva, et al., 2018). A very wide gamma of biomaterials are, nowadays utilized to fabricate scaffolds with 3D printing technologies and their mechanical properties are considerably variable (Wang, Ao, et al., 2016; Chiulan et al., 2017; Ligon et al., 2017). A possible example of thermoplastic material that can be utilized to produce bony tissue scaffolds by means of the selective laser sintering technology and that is characterized by a Young's modulus reasonably close ($E \approx 500$ MPa) to that hypothesized in this article is represented by the Polycaprolactone. Previous studies (Boccaccio, Uva, Fiorentino, Lamberti, et al., 2016; Boccaccio, Fiorentino, et al., 2018) show that reducing (or increasing) the Young's modulus by 50 % leads to predict values of the optimal diameter D approximately and averagely 20 % larger (or smaller, respectively).

In spite of these limitations, the predictions of the models utilized in this study are reasonably consistent with those obtained via other independent ways. In detail, the ratio E_{app}/E between the apparent Young's modulus and the Young's modulus of the material the scaffolds are made from (i.e. $E = 1000$ MPa, see Table 2), was computed for the investigated scaffolds and compared to that obtained via analytical solution. The normalized ratio E_{app}/E is a unit-less parameter typically utilized to study the structural behavior of porous materials or, in general, materials with complex microstructure (Ahmadi et al., 2015). All the analytical solutions utilized for the different unit cells are based on the Euler-Bernoulli theory. Although an analytical solution exists also for the rhombic dodecahedron unit cell (Borleffs, 2012), we could not implement it as it refers to a geometry completely different with respect to that utilized in this paper. The geometry hypothesized by Borleffs (Borleffs, 2012), in fact, can be inscribed in a parallelepiped and includes 12 congruent rhombic faces, our model instead, can be inscribed in a cubic volume (i.e. the volume that we hypothesize to have the dimensions $Q\times Q\times Q$) and includes two families of rhombic faces, one with 4 and the other with 8 congruent rhombic faces. To compute E_{app}, linear elastic models of the sole scaffold (i.e. the granulation tissue model was excluded) were built with diameters D = 40, 60, 80, 100, 120 and 140 μm, clamped on the bottom surface and subjected to a load of p = 0.1 MPa. The resulting displacement u of the top scaffold surface was utilized to determine the quantity E_{app} as: $E_{app} = p / u \times h$. Interestingly, the predicted ratios E_{app} / E are close to those obtained via analytical solutions for small diameters D and tend to diverge as we move towards higher values of diameter (Fig. 13). This behavior can be explained with the fact that the Euler-Bernoulli theory on which the analytical solutions are based, follows the hypothesis that beams are slender (i.e. possess a small diameter). For high values of D, this hypothesis is not anymore satisfied and hence, the difference between analytical and numerical solutions gets larger. Interestingly, this difference is particularly important in the case of the diamond unit cell (Fig. 13). This can be explained with the fact that in the diamond unit cell spherical elements were utilized in correspondence of the connection points (Fig. 2(j)) which obviously, make stiffer the resulting structure. Further details on the analytical solutions implemented to determine the ratio E_{app} / E are reported in the Appendix B.

To date, no experimental studies are reported in the literature that put in relationship the load acting on the scaffold with the amount of the different tissues forming within the scaffold pores. Typically, properties such as pore size, porosity, permeability, specific

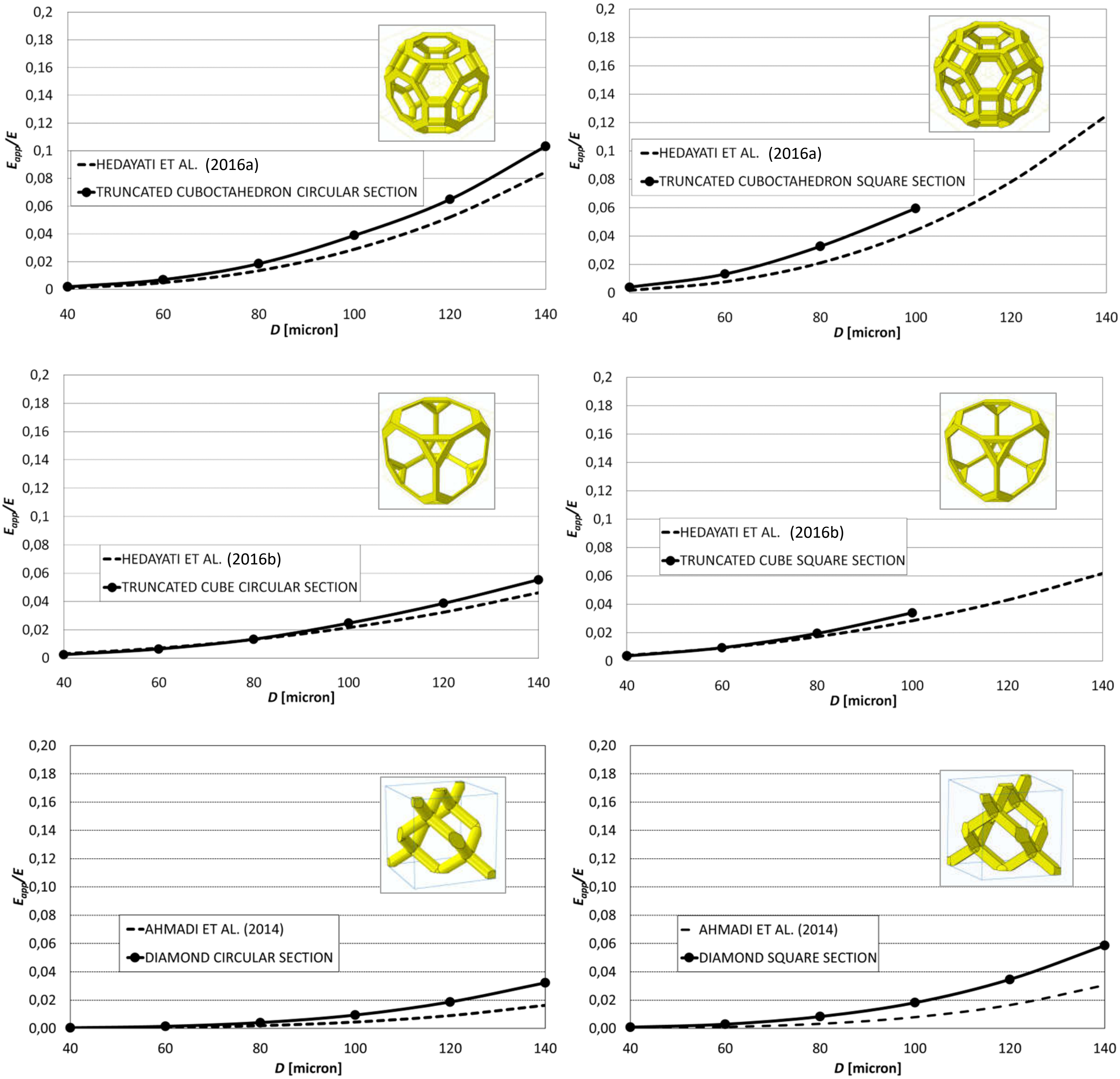

Fig. 13. Corroboration/validation of the scaffold models. The values of E_{app}/E numerically predicted were compared with those computed via analytical solutions. Note. In the diagrams of truncated cuboctahedron and truncated cube unit cells, square cross section, no values are reported for values of $D > D_{max\_i}$.

surface area are measured to evaluate the performance of scaffolds (Wang et al., 2017). For instance, it was found that biodegradable polymeric materials with pores of about 350 µm produce amounts of bone larger than those obtained with scaffolds with smaller pores (Whang et al., 1999). Cheng et al. (Cheng et al., 2014) showed that scaffolds with medium (≈383 µm) and large pore sizes (≈653 µm) are inductive for bone formation. Studies carried out on beam-based regular scaffolds revealed that pore size in the range 400-620 µm are suitable to stimulate metabolic cell activity and migration into the scaffold (Markhoff et al., 2015). Taniguchi et al. (Taniguchi et al., 2016) found that scaffolds based on the diamond unit cell with pore size of 600 µm stimulate the formation of large amounts of bone. Li et al. (Li et al., 2016) showed, for the same unit cell, that pore sizes in the range 300-400 µm have a good performance in repairing bone defects. Many other *in vivo* and *in vitro* studies reviewed by Wang et al. (Wang et al., 2017) found optimal pore sizes that are very similar to those above reported. Interestingly, these pore sizes are consistent with those found in the present study (Table 4). The pore sizes listed in Table 4 were computed according to two different methodologies: (i) for the truncated cuboctahedron, truncated cube and rhombic dodecahedron as the diameter of the largest circular area aligned with a lattice face which is surrounded on the majority of its perimeter by in-plane beams and has no intersections (Arabnejad et al., 2016); (Note. For the diamond unit cell this methodology cannot be used because this cell does not include beams lying in the same plane and circumscribing a circular area); (ii) for the diamond unit cell, as the diameter of the largest sphere that can be fitted in the pore space (Melchels et al., 2010).

Table 4. Computed values of pore size for the different unit cells investigated.

Unit cell	Pore size [μm]
Truncated cuboctahedron	566.23
Truncated cube	576.57
Rhombic dodecahedron	501.58
Diamond	430.00

4. Conclusions

Beam-based scaffolds made from different unit cells were modelled in this study to evaluate their mechanobiological performance. Results show that such scaffolds allow the formation of large amounts of bone for low levels of load, for high values of load, instead, scaffolds based on hexahedron unit cells are preferable. A very intriguing behavior was observed for the truncated cube that was predicted to be the best unit cell for low values of p and the worst one for high levels of load. For low values of load, the diamond was predicted to be the worst unit cell, while for high values, the worst unit cell was the truncated cube. The study can guide the orthopedic surgeon in the choice of the best scaffold to implant into a given anatomic region and provides useful information to the scaffold designers regarding the geometrical constraints and the amount of material needed to build the construct.

Acknowledgements

This research has been made possible thanks to the collaboration between Universidad Nacional de Colombia and Polytechnic University of Bari. It was supported by a PhD grant from Colombian Institute for Science and Research **COLCIENCIAS** (Grant 647-2015).

References

Ahmadi, S., Campoli, G., Yavari, S.A., Sajadi, B., Wauthlé, R., Schrooten, J., Weinans, H., Zadpoor, A., 2014. Mechanical behavior of regular open-cell porous biomaterials made of diamond lattice unit cells. Journal of the mechanical behavior of biomedical materials 34, 106–115.

Ahmadi, S.M., Yavari, S.A., Wauthle, R., Pouran, B., Schrooten, J., Weinans, H., Zadpoor, A.A., 2015. Additively manufactured open-cell porous biomaterials made from six different space-filling unit cells: The mechanical and morphological properties. Materials 8, 1871–1896.

Arabnejad, S., Johnston, R.B., Pura, J.A., Singh, B., Tanzer, M., Pasini, D., 2016. High-strength porous biomaterials for bone replacement: A strategy to assess the interplay between cell morphology, mechanical properties, bone ingrowth and manufacturing constraints. Acta biomaterialia 30, 345–356.

Bobbert, F., Lietaert, K., Eftekhari, A.A., Pouran, B., Ahmadi, S., Weinans, H., Zadpoor, A., 2017. Additively manufactured metallic porous biomaterials based on minimal surfaces: A unique combination of topological, mechanical, and mass transport properties. Acta Biomaterialia 53, 572–584.

Boccaccio, A., Ballini, A., Pappalettere, C., Tullo, D., Cantore, S., Desiate, A., 2011. Finite element method (FEM), mechanobiology and biomimetic scaffolds in bone tissue engineering. International Journal of Biological Sciences 7, 112–132.

Boccaccio, A., Fiorentino, M., Uva, A.E., Laghetti, L.N., Monno, G., 2018. Rhombicuboctahedron unit cell based scaffolds for bone regeneration: geometry optimization with a mechanobiology – driven algorithm. Materials Science and Engineering: C 83, 51–66.

Boccaccio, A., Kelly, D.J., Pappalettere, C., 2011. A mechano-regulation model of fracture repair in vertebral bodies. Journal of Orthopaedic Research 29, 433–443.

Boccaccio, A., Uva, A.E., Fiorentino, M., Lamberti, L., Monno, G., 2016. A mechanobiology-based algorithm to optimize the microstructure geometry of bone tissue scaffolds. International Journal of Biological Sciences 12, 1–17.

Boccaccio, A., Uva, A.E., Fiorentino, M., Monno, G., Ballini, A., Desiate, A., 2018. Optimal Load for Bone Tissue Scaffolds with an Assigned Geometry. International Journal of Medical Sciences, 15, 16–22.

Boccaccio, A., Uva, A.E., Fiorentino, M., Mori, G., Monno, G., 2016. Geometry design optimization of functionally graded scaffolds for bone tissue engineering: A mechanobiological approach. PloS one 11, e0146935.

Borleffs, M., 2012. Finite element modeling to predict bulk mechanical properties of 3D printed metal foams.

Bose, S., Vahabzadeh, S., Bandyopadhyay, A., 2013. Bone tissue engineering using 3D printing. Materials Today 16, 496–504.

Byrne, D.P., Lacroix, D., Planell, J.A., Kelly, D.J., Prendergast, P.J., 2007. Simulation of tissue differentiation in a scaffold as a function of porosity, Young's modulus and dissolution rate: application of mechanobiological models in tissue engineering. Biomaterials 28, 5544–5554.

Campoli, G., Borleffs, M., Yavari, S.A., Wauthle, R., Weinans, H., Zadpoor, A.A., 2013. Mechanical properties of open-cell metallic biomaterials manufactured using additive manufacturing. Materials & Design 49, 957–965.
Cheng, A., Humayun, A., Cohen, D.J., Boyan, B.D., Schwartz, Z., 2014. Additively manufactured 3D porous Ti-6Al-4V constructs mimic trabecular bone structure and regulate osteoblast proliferation, differentiation and local factor production in a porosity and surface roughness dependent manner. Biofabrication 6, 045007.
Chiulan, I., Frone, A.N., Brandabur, C., Panaitescu, D.M., 2017. Recent Advances in 3D Printing of Aliphatic Polyesters. Bioengineering 5, 2.
Coelho, P.G., Hollister, S.J., Flanagan, C.L., Fernandes, P.R., 2015. Bioresorbable scaffolds for bone tissue engineering: optimal design, fabrication, mechanical testing and scale-size effects analysis. Medical engineering & physics 37, 287–296.
Corredor-Gómez, J.P., Rueda-Ramırez, A.M., Gamboa-Márquez, M.A., Torres-Rodrıguez, C., Cortés-Rodrıguez, C.J., 2016. An intramembranous ossification model for the in silico analysis of bone tissue formation in tooth extraction sites. Journal of theoretical biology 401, 64–77.
Dias, M.R., Guedes, J.M., Flanagan, C.L., Hollister, S.J., Fernandes, P.R., 2014. Optimization of scaffold design for bone tissue engineering: a computational and experimental study. Medical engineering & physics 36, 448–457.
El-Rashidy, A.A., Roether, J.A., Harhaus, L., Kneser, U., Boccaccini, A.R., 2017. Regenerating bone with bioactive glass scaffolds: A review of in vivo studies in bone defect models. Acta Biomaterialia 62, 1–28.
Geris, L., Gerisch, A., Vander Sloten, J., Weiner, R., Van Oosterwyck, H., 2008. Angiogenesis in bone fracture healing: a bioregulatory model. Journal of theoretical biology 251, 137–158.
Hedayati, R., Sadighi, M., Mohammadi-Aghdam, M., Hosseini-Toudeshky, H., 2017. Comparison of elastic properties of open-cell metallic biomaterials with different unit cell types. Journal of Biomedical Materials Research Part B: Applied Biomaterials.
Hedayati, R., Sadighi, M., Mohammadi-Aghdam, M., Zadpoor, A., 2016a. Mechanical behavior of additively manufactured porous biomaterials made from truncated cuboctahedron unit cells. International Journal of Mechanical Sciences 106, 19–38.
Hedayati, R., Sadighi, M., Mohammadi-Aghdam, M., Zadpoor, A., 2016b. Mechanical properties of regular porous biomaterials made from truncated cube repeating unit cells: Analytical solutions and computational models. Materials Science and Engineering: C 60, 163–183.
Hendrikson, W., Van Blitterswijk, C., Verdonschot, N., Moroni, L., Rouwkema, J., 2014. Modeling mechanical signals on the surface of μCT and CAD based rapid prototype scaffold models to predict (early stage) tissue development. Biotechnology and bioengineering 111, 1864–1875.
Huiskes, R., Van Driel, W., Prendergast, P., Søballe, K., 1997. A biomechanical regulatory model for periprosthetic fibrous-tissue differentiation. Journal of materials science: Materials in medicine 8, 785–788.
Kang, H., Lin, C.-Y., Hollister, S.J., 2010. Topology optimization of three dimensional tissue engineering scaffold architectures for prescribed bulk modulus and diffusivity. Structural and Multidisciplinary Optimization 42, 633–644.
Keaveny, T.M., Hayes, W.C., 1993. Mechanical properties of cortical and trabecular bone. Bone 7, 285–344.

Li, G., Wang, L., Pan, W., Yang, F., Jiang, W., Wu, X., Kong, X., Dai, K., Hao, Y., 2016. In vitro and in vivo study of additive manufactured porous Ti6Al4V scaffolds for repairing bone defects. Scientific reports 6, 34072.

Ligon, S.C., Liska, R., Stampfl, J., Gurr, M., Mülhaupt, R., 2017. Polymers for 3D printing and customized additive manufacturing.

Loh, Q.L., Choong, C., 2013. Three-dimensional scaffolds for tissue engineering applications: role of porosity and pore size. Tissue Engineering Part B: Reviews 19, 485–502.

Markhoff, J., Wieding, J., Weissmann, V., Pasold, J., Jonitz-Heincke, A., Bader, R., 2015. Influence of different three-dimensional open porous titanium scaffold designs on human osteoblasts behavior in static and dynamic cell investigations. Materials 8, 5490–5507.

Melchels, F.P., Bertoldi, K., Gabbrielli, R., Velders, A.H., Feijen, J., Grijpma, D.W., 2010. Mathematically defined tissue engineering scaffold architectures prepared by stereolithography. Biomaterials 31, 6909–6916.

Murphy, C.M., O'Brien, F.J., Little, D.G., Schindeler, A., 2013. Cell-scaffold interactions in the bone tissue engineering triad.

Olivares, A.L., Marsal, È., Planell, J.A., Lacroix, D., 2009. Finite element study of scaffold architecture design and culture conditions for tissue engineering. Biomaterials 30, 6142–6149.

Polo-Corrales, L., Latorre-Esteves, M., Ramirez-Vick, J.E., 2014. Scaffold design for bone regeneration. Journal of nanoscience and nanotechnology 14, 15–56.

Prendergast, P., Huiskes, R., Søballe, K., 1997. Biophysical stimuli on cells during tissue differentiation at implant interfaces. Journal of biomechanics 30, 539–548.

Roohani-Esfahani, S.-I., Newman, P., Zreiqat, H., 2016. Design and fabrication of 3D printed scaffolds with a mechanical strength comparable to cortical bone to repair large bone defects. Scientific reports 6, 19468.

Sandino, C., Checa, S., Prendergast, P.J., Lacroix, D., 2010. Simulation of angiogenesis and cell differentiation in a CaP scaffold subjected to compressive strains using a lattice modeling approach. Biomaterials 31, 2446–2452.

Sandino, C., Planell, J., Lacroix, D., 2008. A finite element study of mechanical stimuli in scaffolds for bone tissue engineering. Journal of biomechanics 41, 1005–1014.

Sears, N., Touchet, T., Benhardt, H., Cosgriff-Hernández, E., 2012. Tendon and Ligament Engineering.

Taniguchi, N., Fujibayashi, S., Takemoto, M., Sasaki, K., Otsuki, B., Nakamura, T., Matsushita, T., Kokubo, T., Matsuda, S., 2016. Effect of pore size on bone ingrowth into porous titanium implants fabricated by additive manufacturing: an in vivo experiment. Materials Science and Engineering: C 59, 690–701.

Velasco, M.A., Narváez-Tovar, C.A., Garzón-Alvarado, D.A., 2015. Design, materials, and mechanobiology of biodegradable scaffolds for bone tissue engineering. BioMed research international 2015.

Wang, X., Ao, Q., Tian, X., Fan, J., Wei, Y., Hou, W., Tong, H., Bai, S., 2016. 3D bioprinting technologies for hard tissue and organ engineering. Materials 9, 802.

Wang, X., Xu, S., Zhou, S., Xu, W., Leary, M., Choong, P., Qian, M., Brandt, M., Xie, Y.M., 2016. Topological design and additive manufacturing of porous metals for bone scaffolds and orthopaedic implants: a review. Biomaterials 83, 127–141.

Wang, Z., Wang, C., Li, C., Qin, Y., Zhong, L., Chen, B., Li, Z., Liu, H., Chang, F., Wang, J., 2017. Analysis of factors influencing bone ingrowth into three-dimensional printed porous metal scaffolds: A review. Journal of Alloys and Compounds.

Whang, K., Healy, K., Elenz, D., Nam, E., Tsai, D., Thomas, C., Nuber, G., Glorieux, F., Travers, R., Sprague, S., 1999. Engineering bone regeneration with bioabsorbable scaffolds with novel microarchitecture. Tissue engineering 5, 35–51.

Wieding, J., Wolf, A., Bader, R., 2014. Numerical optimization of open-porous bone scaffold structures to match the elastic properties of human cortical bone. Journal of the mechanical behavior of biomedical materials 37, 56–68.

Zadpoor, A.A., Hedayati, R., 2016. Analytical relationships for prediction of the mechanical properties of additively manufactured porous biomaterials. Journal of Biomedical Materials Research Part A.

Appendix A. Definition of the upper bounds

A1. Truncated Cuboctahedron

The upper bound D_{max_1} for the truncated cuboctahedron, circular cross section is defined as the beam diameter for which the square interconnection formed by the orange bars showed in Fig. A.1(a) disappears. This occurs when:

$$D_{max\_1} = L_1 \qquad \text{(A1)}$$

In the case of the square cross section the square interconnection disappears when (Fig. A.1(b)):

$$D_{max\_1} = L_1 \cdot \frac{\sqrt{2}}{2} \qquad \text{(A2)}$$

A2. Truncated Cube

The upper bound D_{max_2} for the truncated cube, circular cross section is defined as the beam diameter for which the triangular interconnection formed by the orange bars showed in

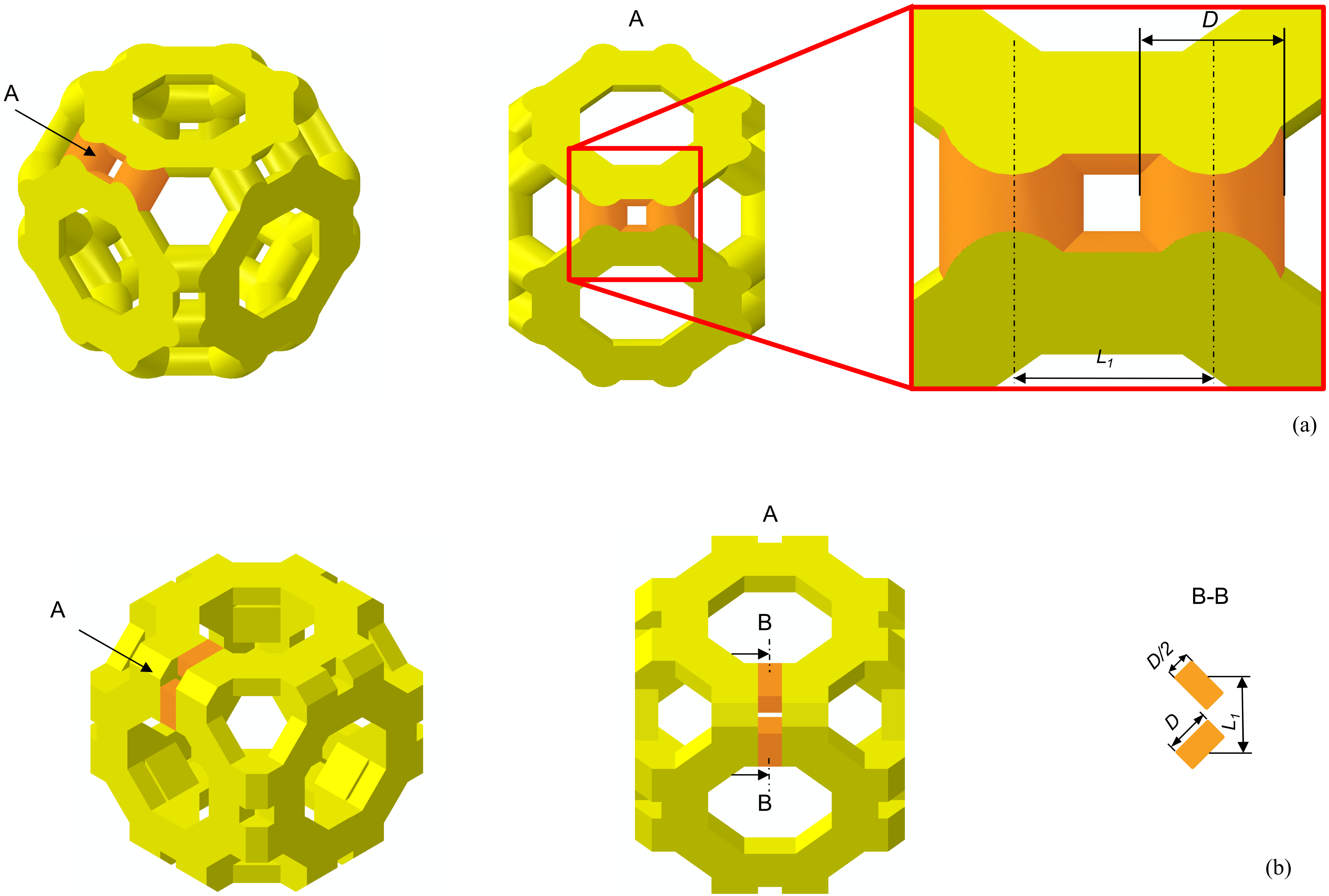

Fig. A.1. Definition of the upper bound D_{max_1} for the truncated cuboctahedron unit cell, circular (a) and square (b) cross section.

the Fig. A.2(a) disappears. If r_c is the radius of the circle inscribed in the triangular interconnection, it follows that this interconnection will disappear when the following relationship is satisfied:

$$D_{max\_2} = 2 \cdot r_c \qquad \text{(A3)}$$

The radius r_c of a circle inscribed in a triangle with area A_T and perimeter P_T is given by:

$$r_c = \frac{2 \cdot A_T}{P_T} \qquad \text{(A4)}$$

Therefore, the following relationship between the upper bound D_{max_2} and the beam length L_2 (Table 1) can be written:

$$D_{max\_2} = 2 \cdot r_c = \frac{L_2 \cdot \sqrt{3}}{3} \qquad \text{(A5)}$$

To compute D_{max_2} in the case of square cross section, the triangular interconnection must be projected onto the lateral plane δ (Fig. A.2(b)). This triangular interconnection will disappear when $D_{max\_2}/2 = r_c$, which leads to the following relationship:

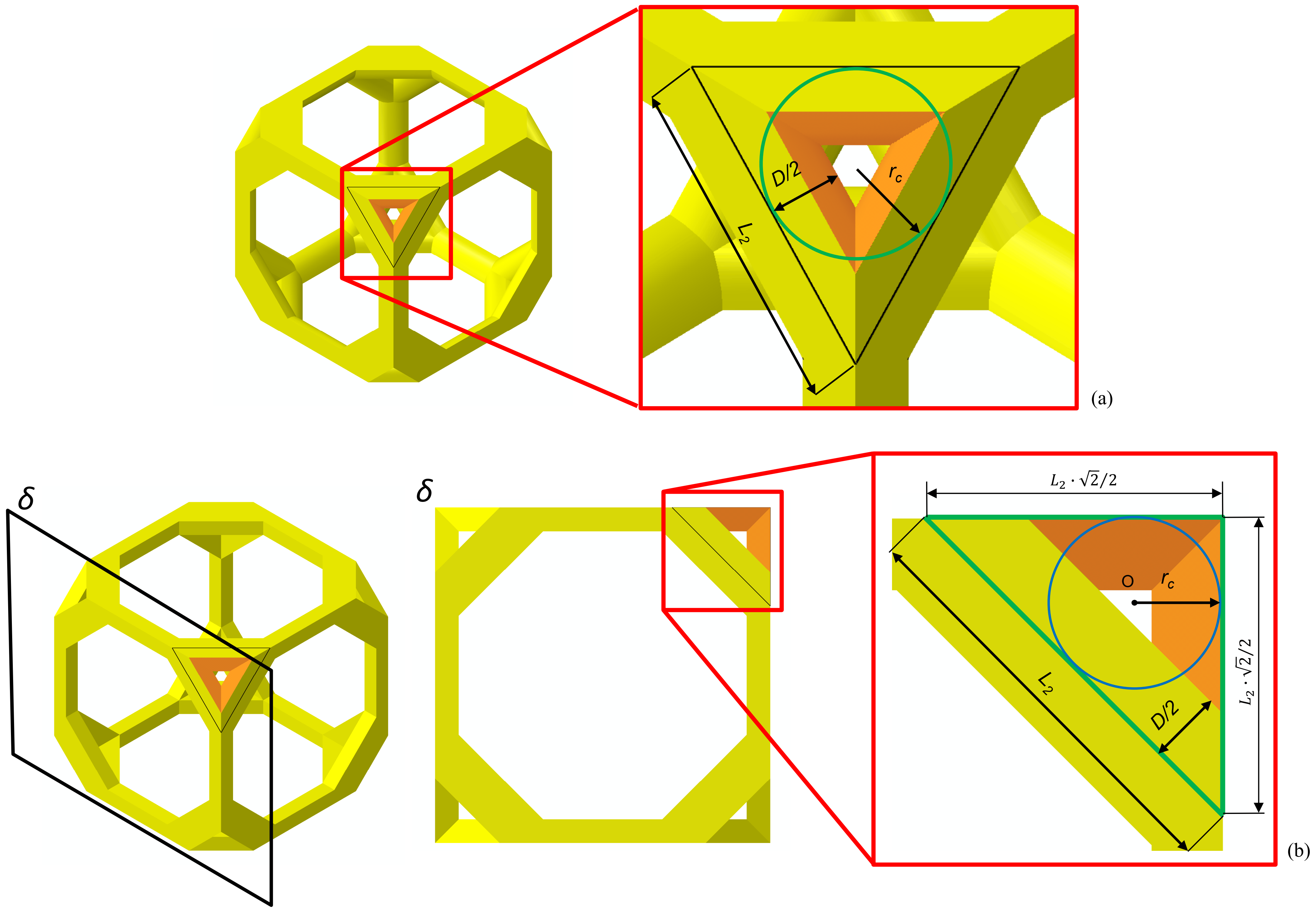

Fig. A2. Definition of the upper bound D_{max_2} for the truncated cube unit cell, circular (a) and square (b) cross section.

$$D_{max\_2} = 2 \cdot r_c = \frac{L_2}{1 + \sqrt{2}} \qquad \text{(A6)}$$

A3. Rhombic Dodecahedron

The upper bound D_{max_3} for the rhombic dodecahedron unit cell with both circular and square cross section is defined as the beam diameter for which the rhombic interconnection shown in Fig A.3(a) disappears. If d is the height of the triangle shown in Fig. A.3(a), the following relationships can be written to compute D_{max_3} in function of the beam length L_3 and the angle α = 53.13°:

$$\begin{cases} d = L_3 \cdot \cos\left(\frac{\alpha}{2}\right) \cdot \sin\left(\frac{\alpha}{2}\right) \\ D_{\max\_3} = 2 \cdot d = 2 \cdot L_3 \cdot \cos\left(\frac{\alpha}{2}\right) \cdot \sin\left(\frac{\alpha}{2}\right) \end{cases} \qquad \text{(A7)}$$

A4. Diamond

The upper bound D_{max_4} of the diamond unit cell with circular cross section is defined as the beam diameter for which the rhombic interconnections (highlighted in orange in Fig. A.3(b)) will disappear. If s is the height of the triangle shown in Fig. A.3(c), the following relationships can be written:

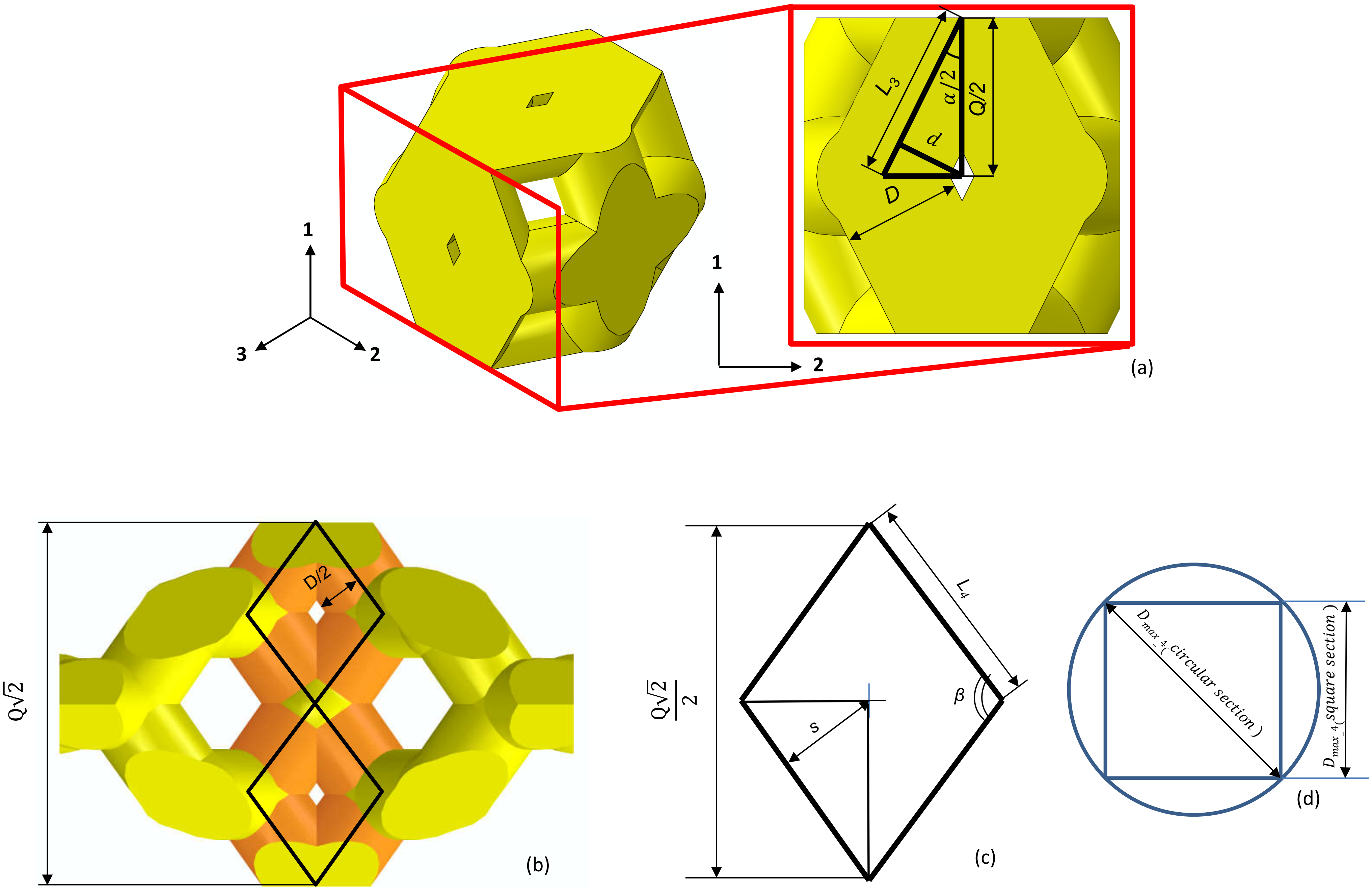

Fig. A3. Definition of the upper bound D_{max_3} and D_{max_4} for the rhombic dodecahedron (a) and the diamond (b-d) unit cell, respectively, with both circular and square cross section.

$$\begin{cases} s = L_4 \cdot \cos\left(\frac{\beta}{2}\right) \cdot \sin\left(\frac{\beta}{2}\right) \\ D_{max\ \_4} = 2 \cdot s = 2 \cdot L_4 \cdot \cos\left(\frac{\beta}{2}\right) \cdot \sin\left(\frac{\beta}{2}\right) \end{cases} \tag{A8}$$

where β = 109.47°

D_{max_4} for the square cross section depends on the orientation of the beams included in the unit cell. However, it is possible to state that in the worst case D_{max_4} for square cross section will be equal to D_{max_4} computed for the circular section (Equation A8) divided by $\sqrt{2}$ (Fig. A.3(d)):

$$D_{max\ \_4} = \frac{2}{\sqrt{2}} \cdot L_4 \cdot \cos\left(\frac{\beta}{2}\right) \cdot \sin\left(\frac{\beta}{2}\right) \tag{A9}$$

Appendix B. Analytical Solutions to Compute E_{app}/E

B1. Truncated Cuboctahedron

According to Hedayati et al. (Hedayati et al., 2016a), the ratio E_{app}/E for the truncated cuboctahedron unit cell is given by:

$$\begin{cases} \dfrac{E_{app}}{E} = \dfrac{18A\beta}{L_1^2(2\sqrt{2}+1)}\left\{\dfrac{(26\alpha+5)+4(296\alpha+69)\beta+864(5\alpha+3)\beta^2}{(16\alpha+3)+72(19\alpha+4)\beta+72(275\alpha+81)\beta^2+9504(5\alpha+3)\beta^3}\right\} \\ \alpha = \dfrac{2I(1+\nu)}{J} \\ \beta = \dfrac{I}{AL_1^2} \end{cases} \quad \text{(B1)}$$

where, L_1 is the beam length, E = 1000 MPa and ν = 0.3 the elastic modulus and the Poisson's ratio, respectively, of the scaffold material (Table 2), A the cross section area, I the area moment of inertia, J the polar area moment of inertia of the beam cross section. In detail, in the case of the circular cross section the following relationships can be written:

$$A = \frac{\pi D^2}{4} \qquad I = \frac{\pi D^4}{64} \qquad J = \frac{\pi D^4}{32} \qquad (B2)$$

while in the case of the square cross section we have:

$$A = D^2 \qquad\qquad I = \frac{D^4}{12} \qquad\qquad J = \frac{D^4}{6} \qquad \text{(B3)}$$

B2. Truncated Cube

According to Hedayati et al. (Hedayati et al., 2016b), the ratio E_{app}/E for the circular cross section is given by:

$$\frac{E_{app}}{E} = \frac{2\pi}{(\sqrt{2}+1)}\left(\frac{D}{2L_2}\right)^2 \frac{1+9\left(\frac{D}{2L_2}\right)^2}{5+21\left(\frac{D}{2L_2}\right)^2} \qquad (B4)$$

In the case of the square cross section, instead, we have:

$$\frac{E_{app}}{E} = \frac{2}{(\sqrt{2}+1)}\left(\frac{D}{L_2}\right)^2 \frac{1+3\left(\frac{D}{L_2}\right)^2}{5+7\left(\frac{D}{L_2}\right)^2} \qquad \text{(B5)}$$

B3. Diamond

According to Ahmadi et al. (Ahmadi et al., 2014) the following relationship exists between the ratio E_{app}/E and diamond unit cell geometrical parameters:

$$\begin{cases} \dfrac{E_{app}}{E} = \dfrac{\rho^2}{3.85 + 1.41\rho} \\ \rho = 1.02\,\dfrac{D^2}{{L_4}^2} \end{cases} \qquad \text{(B6)}$$

being ρ the apparent density for the diamond structure.

Figure legends

Fig. 1. Steps followed to build the truncated cuboctahedron unit cell (a-e). An octagonal trajectory t_1 was first traced. Then, a sweep of the circular or a square cross section was performed along t_1 thus obtaining a solid sub-unit including eight beams (a). Two axes (a_{1_x} and a_{1_y}) were hence defined and through rotation operations around them the original solid sub-unit was replicated five times (b). The resulting disconnected sub-units were finally connected by means of beams (c). The unit cell so generated was cut along the planes π_{M1}, π_{M2}, …π_{M6} thus obtaining the final unit cell: circular (d) and square (e) cross section. Steps followed to build the truncated cube unit cell (f-i). After building the first solid sub-unit (f), two axes were defined (a_{2_x} and a_{2_y}, (g)) and replications of the original sub-unit were performed by rotating it around a_{2_x} and a_{2_y}. The unit cell so obtained was cut along the same planes π_{M1}, π_{M2}, …π_{M6} delimiting the cubic volume $Q\times Q\times Q$ ((h) circular cross section, (i) square cross section).

Fig. 2. Steps followed to build the rhombic dodecahedron unit cell (a-g).A rhombic trajectory t_3 was first traced and the sweep of a circular or a square section was then performed (a) thus obtaining a first solid sub-unit. After defining the axis a_{3_x} (b), three replications of the initial sub-unit were obtained by rotating it around a_{3_x} by the angles $\pi/2$, π and $3\pi/2$. To link completely the cell, half sub-units were finally added that lie in the horizontal plane π_H (c) and in the vertical plane π_V (d). The resulting unit cell was finally cut along the faces of the planes π_{M1}, π_{M2}, …π_{M6} ((e) circular cross section, (f) square cross section). In order to evaluate the effect of the cell orientation, the same rhombic topology with a rotation of $\pi/2$ was modelled (g). Steps followed to build the diamond unit cell (h-n). This unit cell was built by performing the protusion of the cross section along linear paths (h) inclined one each other by the angle β = 109.47°. In order to guarantee the continuity (i) between the single beams connections spheres were included in the model (j). Once the unit cell was built, it was properly oriented to have the vertices V_1, V_2, V_3 and V_4 coincident with those of the cubic volume $Q\times Q\times Q$ (k). Cuts were finally performed along the faces of the planes π_{M1}, π_{M2}, …π_{M6} ((m) circular cross section, (n) square cross section).

Fig. 3. Boundary and loading conditions acting on the scaffold model (a). Exploiting the symmetry of the problem, the volume analyzed was reduced to one quarter of the total volume (b). Symmetry constraints were utilized on the faces of the model lying on the symmetry planes $\pi_{1\text{-}2}$ and $\pi_{3\text{-}2}$ where the absence of any fluid flow was imposed ((b) and (c)).

Fig. 4. Scaffold and granulation tissue models (first two columns) and finite element mesh utilized (second two columns).

Fig. 5. Schematic of the algorithm written in Matlab environment to determine the optimal dimension D for different unit cell geometries.

Fig. 6. Optimization of the truncated cuboctahedron unit cell. (a) Optimal scaffold geometries predicted for circular (top) and square (bottom) cross section. Values of the optimal diameter D (b) and of $BO_{\%MAX}$ (c) predicted for different levels of load.

Fig. 7. Optimization of the truncated cube unit cell. (a) Optimal scaffold geometries predicted for circular (top) and square (bottom) cross section. Values of the optimal diameter D (b) and of $BO_{\%MAX}$ (c) predicted for different levels of load.

Fig. 8. Optimization of the rhombic dodecahedron unit cell. (a) Optimal scaffold geometries predicted for circular (top) and square (bottom) cross section. Values of the optimal diameter D (b) and of $BO_{\%MAX}$ (c) predicted for different levels of load.

Fig. 9. Comparison between two different unit cell orientations: Orientation A and Orientation B (a). Values of $BO_{\%MAX}$ (b) and of the optimal diameter D (c) predicted by the algorithm for different levels of load and for the two different cell orientations.

Fig. 10. Optimization of the diamond unit cell. (a) Optimal scaffold geometries predicted for circular (top) and square (bottom) cross section. Values of the optimal diameter D (b) and of $BO_{\%MAX}$ (c) predicted for different levels of load.

Fig. 11. Comparison of the amounts of bone $BO_{\%MAX}$ predicted to form for different unit cell geometries (a) with both circular (b) and square (c) cross section. In order to improve the visualization of data, a logarithmic scale was utilized on the axis of the load.

Fig. 12. Percentage of volume occupied by mature bone, scaffold and other tissues predicted for truncated cuboctahedron (a), truncated cube (b), rhombic dodecahedron (c) and diamond (d) unit cells. For the sake of brevity, the only results regarding the circular cross section are reported. Note. The percentage occupied by mature bone is the same quantity so far denoted as $BO_{\%MAX}$.

Fig. 13. Corroboration/validation of the scaffold models. The values of E_{app}/E numerically predicted were compared with those computed via analytical solutions. Note. In the diagrams of truncated cuboctahedron and truncated cube unit cells, square cross section, no values are reported for values of $D > D_{max\_i}$.

Fig. A.1. Definition of the upper bound D_{max_1} for the truncated cuboctahedron unit cell, circular (a) and square (b) cross section.

Fig. A.2. Definition of the upper bound D_{max_2} for the truncated cube unit cell, circular (a) and square (b) cross section.

Fig. A.3. Definition of the upper bound D_{max_3} and D_{max_4} for the rhombic dodecahedron (a) and the diamond (b-d) unit cell, respectively, with both circular and square cross section.